AN ABSTRACT OF THESIS OF

Walter James Williams for the degree of Master of Science in Radiation Health Physics presented on May 30,2013

Title: Neutron Radiography And Tomography: Determining And Optimizing Resolution Of Neutron Sensitive Multi Channel Plate Detectors

Abstract Approved:_____
Steven R. Reese

The objective of this work was to determine and optimize the resolution of a neutron sensitive Multi-Channel Plate (MCP) detector in order to determine its capabilities in radiography and tomography. The Oregon State University, Neutron Radiography Facility added an MCP Detector in 2012 in order to analyze these capabilities. The leading factor in the generation of both two-dimensional and three-dimensional imaging was the spatial resolution of the detector. The MCP detector developed by Nova Scientific Inc. uses the $^{10}B(n,\alpha)Li^{7}$ reaction within the MCP's bulk walls in order to convert the neutron into an α and lithium particle which have a high probability of initiating an electron avalanche that generates an output pulse. This reaction

governs the spatial resolution. The detector's mechanics allow for a theoretical maximum spatial resolution of 17 μm. By fine tuning the electronics and using a thermal neutron beam, count rates can be recorded throughout the active detector area, where lower count rates can be used to identify areas of neutron absorption or attenuation within the object. These differences are used to create a radiograph which gives information on the material's attenuation coefficient and geometry of the object being imaged. For this study, the objects include resolution masks, American Society for Testing and Materials (ASTM) Standards, along with a variety of other materials. Since the radiograph is digitally created in near real-time, the detector has the capability of neutron tomography with the radiograph's resolution being on the order of the theoretical limit.

Neutron Radiography And Tomography: Determining And Optimizing Resolution Of Neutron Sensitive Multi Channel Plate Detectors

By

Walter James Williams

A THESIS

Submitted to

Oregon State University

in partial fulfillment of

the requirements for the

degree of

Master of Science

Presented May 30, 2013

Commencement June 2014

Master of Science thesis of Walter James Williams presented on May 30, 2013

APPROVED:

Major Professor, representing Radiation Health Physics

Head of the Department of Nuclear Engineering and Radiation Health Physics

---

Dean of the Graduate School

I understand that my thesis will become part of the permanent collection of Oregon State University libraries. My signature below authorizes release of my thesis to any reader upon request.

Walter James Williams, Author

ACKNOWLEDGEMENTS

I would like to thank all of my friends, family, colleagues and advisors for the support. Special thanks to Dr. Reese for helping out through the ups and downs. I would also like to thank Idaho National Labs for funding my Graduate Research Assistantship at Oregon State University.

TABLE OF CONTENTS

TABLE OF FIGURES

LIST OF TABLES

1 Introduction

The Oregon State University's (OSU), Neutron Radiography Facility (NRF) added a multi-channel plate (MCP) Detector in 2012 in order to create neutron radiographs and tomographs and analyze these capabilities. The leading factor in the generation of both two-dimensional and three-dimensional imaging is the spatial resolution of the detector. The MCP detector developed by Nova Scientific Inc. uses the $^{10}B(n,\alpha)Li^{7}$ reaction within the MCP's bulk walls in order to convert the neutron. The α particle has a high probability of initiating an electron avalanche within the MCP channels, which generates the output pulse. This reaction governs the spatial resolution, as the track lengths of the α and lithium nuclei within the detector are approximately 4 μm. The time delay of the pulse is used to back calculate the location of the interaction with spatial resolution of approximately 9 μm. This allows for a theoretical maximum spatial resolution of 17 μm. By fine tuning the electronics and using a thermal neutron beam, count rates can be recorded throughout the active detector area, where lower count rates can be used to identify areas of neutron absorption or attenuation caused by an object within the beam. These differences are used to create a radiograph which

gives density information on the material and geometry of the object being imaged.

The NRF uses a thermal neutron beam from the TRIGA® reactor at OSU. This beam is heavily collimated and filtered with boron and sapphire to remove a majority of the gamma particles from the beam while shaping it into a parallel beam. The beam has a thermal neutron flux of approximately 4.6E5 n cm^{-2} s^{-1} with an L/D ratio of 100 at the detectors location

While neutron radiography is already common practice, neutron tomography is not. Radiography works in two dimensions by measuring some attenuation of radiation after it has passed through an object as shown in Figure 1 below. The cause of the attenuation cannot be distinguished between the thickness or the density of the object.

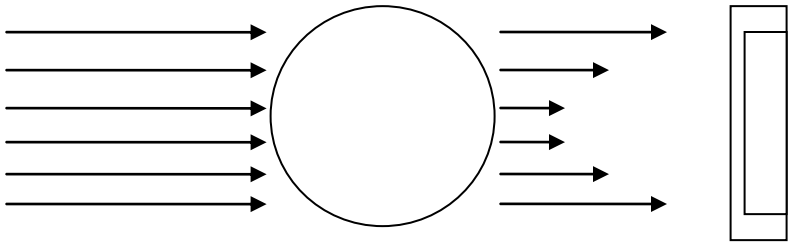

Figure 1: Attenuation Of Uniform Radiation Beam

Due to the inability to make these distinctions, all of the information about the object is compressed into a single geometric plane. In contrast, tomography has the ability to view this same object in three-dimensions. This is done by taking a series of radiographs of the object at different known angles and reconstructing these images to form a tomograph.

1.1 Purpose

The purpose of this research was to analyze a new high-resolution neutron imaging system that uses a MCP based detector to generate radiographs in near real-time. The analysis consisted of the following: determining its resolution in neutron imaging, the capabilities of the modified MCPs and their ability to allow neutrons to cause a detectable electron avalanche within the detector, the practicality of performing neutron tomography with such a detector, and time constraints on collecting images. The system in use at OSU ideally would have a resolution of on the order of 30 micron if the divergence of the beam is sufficiently low and the sample can be placed close to the MCP detection element.

1.2 Objective

For this study, radiographs were taken of objects including resolution masks, ASTM standards, along with a variety of other materials. These images and standards were used to establish the spatial resolution of the detector in order to determine its capabilities and practicality in neutron imaging. Likewise, the standards' were also used to ascertain the quality of a neutron detectors radiograph. The two standards used were a Beam Purity Indicator (BPI) and a Sensitivity Indicator (SI) (1).

Since the radiograph was digitally created in near real-time, neutron tomography was tested for practicality and whether the radiographs resolution was on the order of the theoretical limit. The system was shown to produce radiographs with a resolution an order of magnitude lower that most existing high-speed neutron radiography systems.

1.3 Document Overview

This paper is organized in the following manner:

Chapter 1: Introduction - The introduction discusses the purpose and objective of this thesis.

Chapter 2: Survey of Literature - The survey of literature discusses previous work in the field of radiography and tomography and current methods for analyzing detectors for their imaging capabilities.

Chapter 3: Materials and Methodology - Materials and Methodology is a detailed description of the procedure used to fulfill the purpose and objective of this thesis.

Chapter 4: Conclusion and Discussion - Conclusion and Discussion covers the determined resolution and practicality of this detector and applications, along with concluding remarks concerning this thesis.

2 Survey Of Literature

This section is separated into two parts. The first being a survey on the history of radiography and tomography. The second is a survey on methods for determining spatial resolution of the detector.

2.1 History

Neutron radiography and tomography are used to describe the production of two-dimensional and three-dimensional images by transmitting neutrons through an object and onto a neutron sensitive film or detector. The neutron was first proposed by Rutherford in the early 1900's. He postulated that there was a particle that was able to move through materials more freely than electrons. However, it would be exceptionally difficult to detect due to the nature of its interactions and not being affected by charge (2).

W.D. Harkins was credited for giving the neutron its name while writing a classification of isotopes in 1921 (3). However it was not until 1932 that James Chadwick discovered the neutron while examining the emission of α particles and working with beryllium. He found it to be a highly energetic

and penetrating particle. This discovery ultimately lead to Chadwick receiving the Nobel Prize (4) (5).

Not long after this ground breaking discovery, and only forty years after the first radiograph from x-rays, people began searching for applications for neutrons. The first demonstration of neutron imaging was done by Hartman Kallmann and E. Kuhn in 1935, when they used a small neutron accelerator to create the first radiograph using neutrons (6). This source was a continuous yield neutron generator that used the $H^3(d,n)He^4$ reaction in a miniature sealed tube accelerator to generate an output of fast neutrons from a collision of a mixed beam of deuterium and tritium ions with a deuterium-tritium loaded target (7).

Neutrons are efficiently attenuated by only a few specific elements such as hydrogen, boron, cadmium, samarium and gadolinium. Neutron radiography is an advance technique for non-destructive testing of materials and is exact analogue of X-ray radiography; a method based on the local variations in absorption encountered by a beam in simple transmission. Any inhomogeneity, or neutron absorption and scatter properties, of the object such as internal structure, defects like voids, cracks, inclusions, and porosity

will be shown up as a change in the detected intensity recorded behind the object. It is possible to investigate very bulky objects and selectively see those parts with high real or apparent absorption cross-section and also inspects large thicknesses of heavy materials by neutrons in much less time than required by X-ray radiographs. Therefore, it has some special advantages in nuclear, aerospace, ordnance and rubber & plastic industries (8).

During this same time, O.Z. Peter was using a more powerful neutron generator to produce radiographs of his own. His method cut down the needed beam time from the hours that Kallmann and Kuhn required, to only minutes. This research was set back by the onset of World War Two and was not able to be continued or published until 1946, after the war had ended (9). The Manhattan Project provided many advances in the nuclear industry, such as reactors that allowed for a larger neutron flux than other sources. This lead to more practical research in this field by creating thermal neutron fluxes many orders of magnitude higher than those produced from previous neutron generators. It was at this point that the opportunity for the application of neutrons in non-destructive imaging started to come to light. Its first realistic use was looking for voids in uranium, something that was not previously possible due to the heavy attenuation of x-rays within high Z materials. With

the advent of reactor technology, it was J Thewlis in England that was able to take the first neutron radiographs of useful quality (10).

In early 1960, Harold Berger and John Barton simultaneously began evaluating neutrons as a tool for investigating irradiated reactor fuel. This was done primarily at Argonne National Laboratories (11). This was where Watts was able to produce the first American radiographs. Over the previous few years, it became common knowledge amongst the scientific community that neutron imaging was best achieved, in fact nearly impossible without, using reactors(12).

By the 1970's most reactors designated for research throughout Europe and the United States were able to take neutron radiographs of reasonable quality (13). In order to further develop and improve the methods and quality of these radiographs, a meeting was held in Birmingham, England in 1973 and again in Gaithersburg, USA in 1975. These conferences aided in the advancement of neutron imaging techniques by pooling methods and results from across the world (14).

In 1979 the Neutron Radiography Working Group was formed; its first meeting being held in Riso, Denmark, through the Commission of the

European Communities. The second World Conference was held in 1987 in Paris, France (15). Papers discussed at these meetings suggested the development of electronic real-time neutron radiography, something not achieved until the late 1980's. This was done using newly developed detectors for the time, but more importantly, medium to high flux reactors with well-defined neutron beams (16).

2.2 Instrumentation

Once neutron sources became more available, the next real stepping stone was instrumentation available to record and process detected neutrons into better radiographs. Radiographs can be taken using different techniques, each of which provides different information. In order to determine which method is appropriate, it is first important to note the radiation type. By the time neutron radiography came to be, x-ray radiography was already well established. X-rays are attenuated as they pass through or near an atoms electron cloud, losing energy or being absorbed along the way through pair production, Compton scattering, and the photoelectric effect. Detectors are used to ascertain details about the object imaged by comparing attenuated radiation to that of the uniform beam.

Neutrons however, interact much differently than x-rays. While ionizing electromagnetic radiation interacts with the electron clouds, neutrons are only interacting with nuclear forces. This difference is reflected in their absorption coefficients. X-rays absorption coefficients are directly related to the size of the atoms and the electron cloud, best represented by the atomic number, thus x-ray imaging becomes impractical for higher atomic number

materials. Neutrons, interacting with the nuclear forces, do not follow this log-linear trend. They instead follow a seemingly random trend when comparing their absorption coefficients to the atomic number of a material, shown in Figure 2.

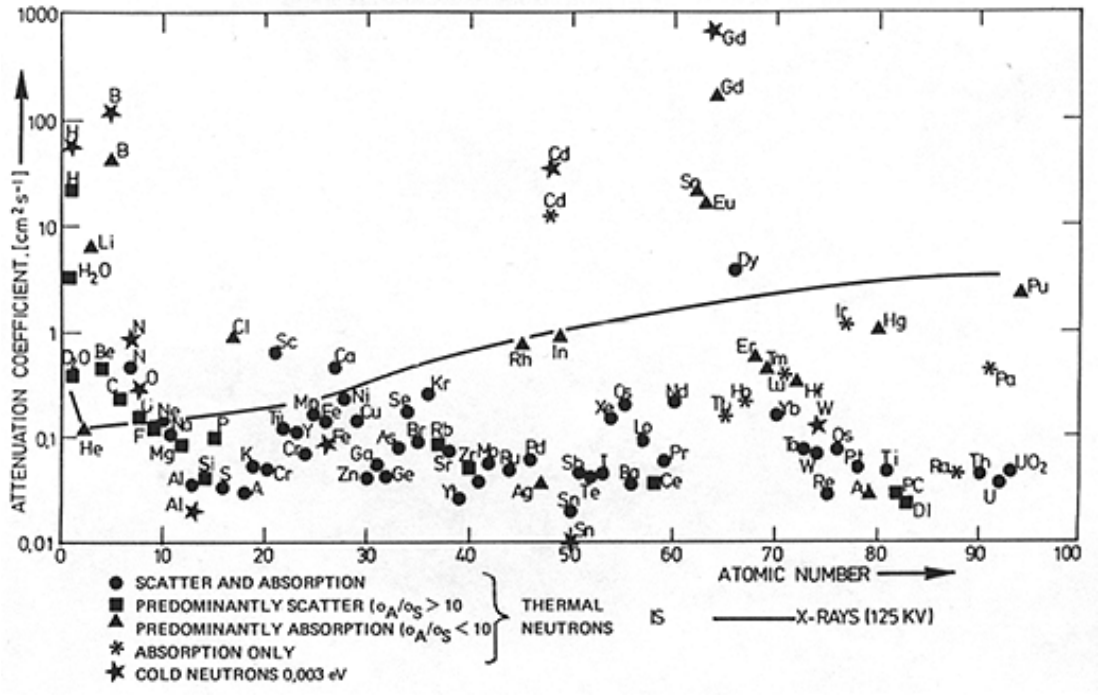

Figure 2: Attenuation Coefficients Of Neutrons And X-Rays (17)

The attenuation coefficients, μ, are calculated using the cross sections, σ, of the specific isotopes and the atomic density of the isotope, N, as shown in the equation $\mu = \sigma * N$. The cross section, the main concern of this work, is the sum of the scattering cross section and the absorption cross section. The two interactions create the varying trend in Figure 2. Neutrons interacting

through absorption can be seen following somewhat of a log-linear trend similar to x-rays, but since neutrons interact with the nuclear potential of the isotope, the cross section also varies by isotope. An example of this is hydrogen having a cross section nearly ten times larger than that of deuterium where H^1 has an incoherent scattering cross section of ~80 barns while deuterium has an incoherent scattering cross section of ~2 barns (18).

This causes neutrons to be much harder to detect as the detectors must consist of materials that can capture neutrons effectively. Thus it is easier to convert neutrons into other particles that can be recorded. Converting the neutron to an x-ray and using photographic film is one technique. Photographic film works by using intensifying screens that convert the X-ray to light, which then produce a visible pattern on the film. However, typical photographic films are nearly unaffected by neutrons. Because of this, a converter is placed over the film. The converter screen can be used during the exposure or post exposure depending on the type of converter. When this is done during the exposure, it is called direct exposure. When it is done post exposure, it is called indirect, or transfer(17). An example of the direct technique is shown in part A of Figure 3. This is where a gadolinium screen is placed onto a photo-sensitive film and exposed in a neutron beam. Once the

neutrons interact with the Gadolinium, the following reaction occurs ^{157}Gd(n,gamma)^{158}Gd. In this case, electron capture is used to produce the prompt particle emission resulting from the neutron interaction. For a Gd converter, this is an internal conversion electron that creates a photographic image upon the film.

The indirect, or transfer, method is shown in part B of the Figure 3. This is done by exposing only the dysprosium converter screen to the neutron beam and then placing it upon the photo sensitive film post irradiation. The film then generates a radiograph by capturing the Beta particle the decay of $^{165}\mathrm{D} \rightarrow \beta + {}^{165}\mathrm{Ho}$ following the ^{164}Dy(n,gamma)^{165}Dy reaction (19).

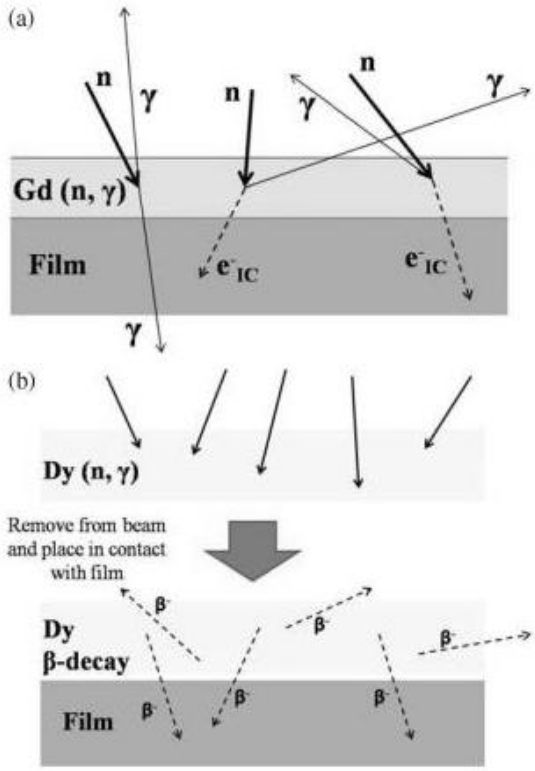

Figure 3: Film Radiography Reactions (19)

These methods can have a resolution on the order of tens of μm (19). While their resolution is competitive, they lack the speed to perform practical tomography, taking long times to acquire multiple images. This is because each radiograph requires the removal and replacement of films and converter screens, after which each film must be developed.

Another neutron radiography detection method involves scintillation based detectors. The neutron radiography facility at the National Institute for Standards and Technology (NIST) uses a scintillation light converter screen, a

mirror, a condensing lens and a CCD camera to perform neutron radiography. This is used for radiography by reflecting the scintillation light out of the beam path using a mirror and focusing this light onto a CCD camera. This method allows for very fast acquisition of images with a high fluence thermal neutron beam. This high speed was capable of collecting images for tomography; however, with a spatial resolution of approximately 200 μm, high precision tomography is not yet possible with this scintillation detector (21).

Simultaneously, other detectors were being implemented in order to transform radiography facilities into tomography capable facilities. One example of this was done at the BATAN's RSG-GAS Reactor in Indonesia. This facility used a CCD camera and an L^6ZnS scintillator screen along with a TiO_2 mirror. This facility is currently able to utilize their high flux neutron beam on the order of 1E6 [ncm^2s^{-1}] to carry out tomography scans in times of around thirty minutes (22).

In January 2006 NOVA Scientific developed a neutron sensitive MCP to perform neutron radiography, which was tested at NIST. The work done there resulted in a measured spatial resolution of approximately 15 μm. This

was the highest resolution measured with a high-speed neutron sensitive radiographic imaging system. While the resolution was comparable to or higher than other modern systems, the detector efficiency was calculated to be relatively low compared to other system at 18-20% efficiency (23).

This MCP system was made up of thin glass disks with microscopic holes running through them. These holes run in parallel to make an array of millions of close-packed hollow glass tubes with diameters from 4 to 100 μm, where each capillary is an independent, microscopic channel electron multiplier. There has been extensive testing done at UC Berkeley on the physics behind MCP detectors. These tests have resulted in a proposed maximum spatial resolution of approximately 15 μm. While the detector efficiency is not yet precisely determined, they have performed calculations showing that a stack of multiple MCPs can yield detection efficiencies upwards of 78%. However, unlike the detectors in production, this would require more than two multi channel plates, and possibly upwards of five. (24)

While detector development play an important role in the acquisition of neutron radiographs, the source being used to acquire them can be said to play just as important of a role. The most common source utilized today is a neutron beam from a nuclear reactor. These beam ports are being drastically

improved by advancements in collimators being implemented as well as the orientation of the beam with respect to the reactor. Both of these allow for lower gamma content of the beam as well as having a heavily thermal beam instead of a fast neutron source. The lower gamma content is vital due to the fact that many neutron event counting detectors are sensitive to gamma radiation as well. The use of cold and thermal neutrons is vital because the absorption coefficients of fast neutron are much lower and therefore harder to accurately detect (25).

3 Materials And Methods

3.1 Detector And Electronics

MCP imaging detectors with high spatial resolution and timing accuracy are already widely used for electrons and ions, as well as UV and X-ray photons. However, it was not until recently that MCPs became applicable to neutron detection with high two-dimensional spatial resolution. This was done by adding boron, specifically ^{10}B to the MCP glass structure to enhance the neutron interaction within the MCP through the $^{10}B(n,\alpha)^{7}Li$ reaction, illustrated in Figure 4. This reaction produces Li-7 (1.01 MeV) and a recoil α particle (1.8 MeV) with a branching ratio of 6%, or Li-7 (0.84 MeV) and an α particle (1.47 MeV) and a gamma ray (0.48 MeV) with a branching ratio of 94%. (23)

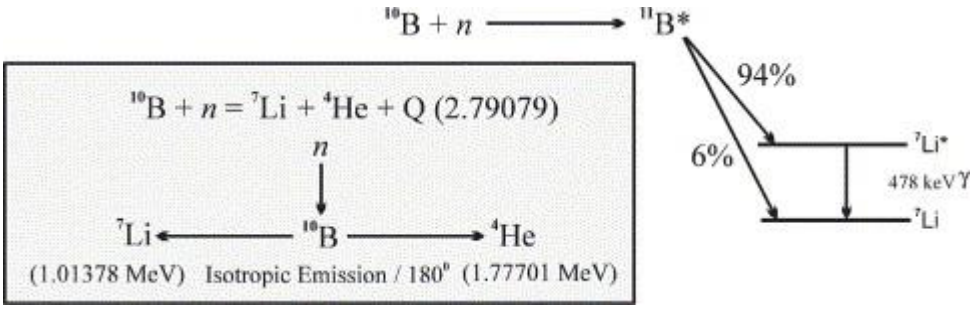

Figure 4: Boron Neutron Interaction (24)

These reaction products, primarily the α particle, create secondary electrons directly in MCP channels through ionizations within the channel walls, which in turn initiates an electron avalanche and a subsequent strong output pulse. The α particle has a very short range, approximately 3.5 μm within the MCP glass, and a very high probability of initiating an electron avalanche, while the ^{7}Li is absorbed within the glass walls due to its higher LET. The geometry of these reactions within the MCP detector is illustrated in Figure 5.

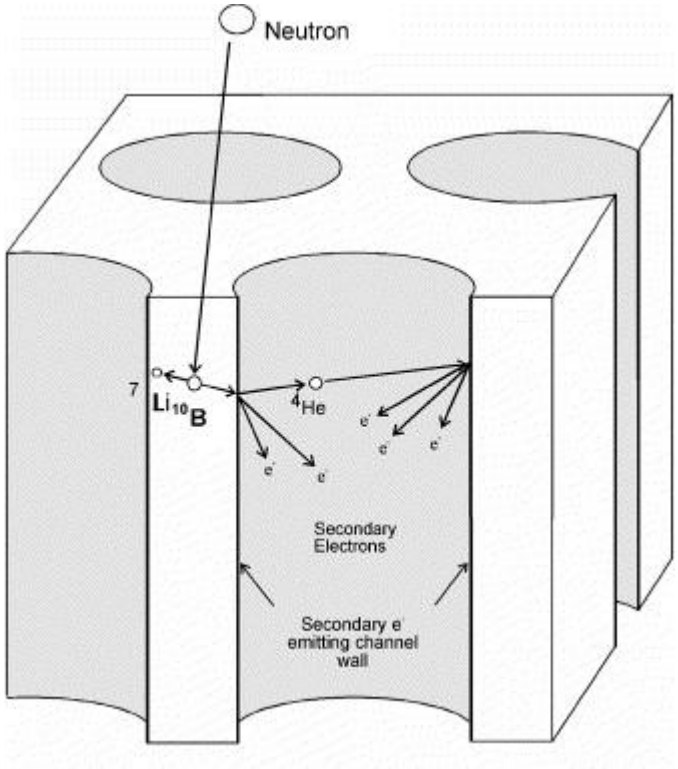

Figure 5: Electron Avalanche (24)

The neutron reactions primarily occur in the forward most MCP, where this MCP provides a gain of 10E6 to 10E7e^-. A delay line anode then captures the electron cloud from the MCP stack and integrates the electrons as a charge. This allows for the signal to be interpreted by user controlled electronics and an event location can then be calculated, producing a spatial resolution of 9 μm. The track length of the α particle, 3.5 μm, can be in any direction, giving a spatial resolution of ~7 μm. Summing the two values gives a theoretical maximum neutron event spatial resolution of approximately 15 μm.

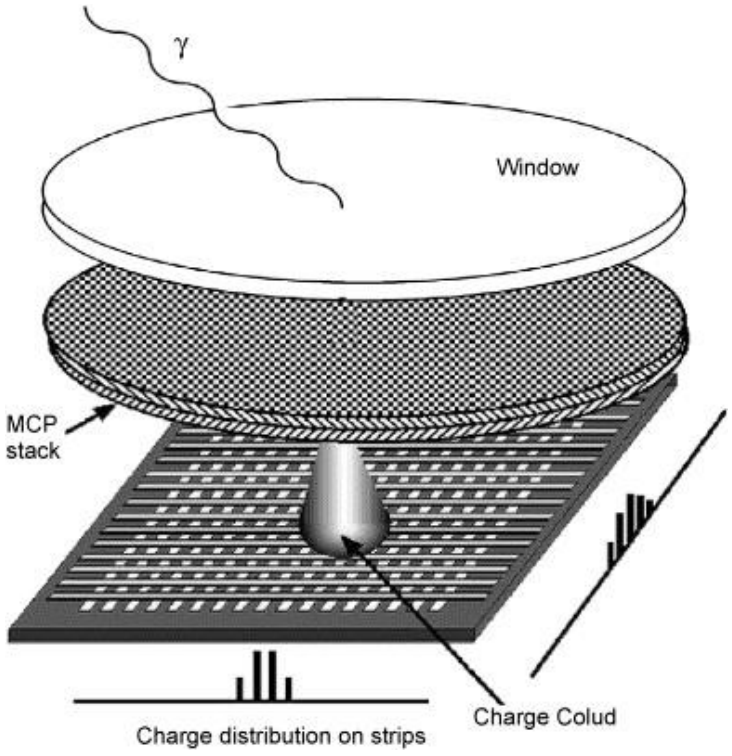

Figure 6: MCP/Anode Layout (23)

The neutron detection efficiency, Q_n, of a ^{10}B-doped MCP detector is given by the product of three terms, Q_n=P1*P2*P3 where P1 is the fraction of incident neutrons absorbed by the MCP structure, P2 is the fraction of those interactions that generate an electron avalanche within an MCP channel, and P3 is the fraction of avalanches registered by the electronics. Due to the extremely sensitive electronics, an electron avalanche always yields a detectable electron pulse, resulting in P3=1. Therefore, the primary detection process consists of the multiplication of the first two terms P1 and P2. The value of P3 relies upon the MCP detector operation and user control (24). This control consists of using appropriate bias voltages, configuring MCPs in a proper configuration, as well as the threshold range of the pulse readout electronics. Due to the fact that this is a high speed detection system, optimizing these factors is very practical because the effect of the adjustments is shown instantly.

P1, the probability of absorption, and P2, the probability of initiating an avalanche, have been judiciously calculated by Downing, Feller, and Tresmin (24). While the final Q_n was measured, P1 and P2 were not individually measured in this study.

Working under the assumption that the P3 value has been optimized, the product of P1 and P2 were determined by first calculating the rate of neutrons incident on the detector. This was calculated in the equation below by multiplying the neutron flux, with the active area of the detector.

$$4.6 * 10^5 \frac{neutrons}{cm^2 s} * \pi * (1.25cm)^2 = 1.8E6 \frac{neutrons}{s}$$

Using this value, and comparing it to the maximum count rate achieved after the removal of noise, approximately 2.5E5 neutrons s^{-1}, the product P1 and P2, and therefore total efficiency, was calculated below to be approximately 14%.

$$Q_n = P1 * P2 * P3 = \frac{2.5E5 \frac{neutrons}{s}}{1.8E6 \frac{neutrons}{s}} * 100 = 14\%$$

3.2 Configuring The Electronics

As discussed, the electronics play a significant role in MCP detector systems. In order to optimize detection efficiency, the first step requires setting the voltage bias across the detector plates using the main power supply. Because the detector is operated within a vacuum, ranging from 10E-6 to 10E-8 torr, no single voltage bias can be assumed to be the correct value. However, so long as the vacuum is within this operating range, a starting

point of 1800 Volts and 2900 Volts applied to the back and front plates respectively will start yielding counts within the detector. At this point, with all of the system thresholds minimized to allow for all events, the bias should be raised in small windows of 20 V increments without exceeding a voltage gap of more than 1200 or exceeding 3200 V on either plate, until the event count rate is optimized. The next step, done visually, is to adjust the thresholding and timing within preamplifier, constant fraction discriminator, and time delay card. Again, this is not a set value. Three examples, shown in Figure 7, show the effects of threshold adjustments. The color gradient represents registered counts at that location and should be equalized as best as possible.

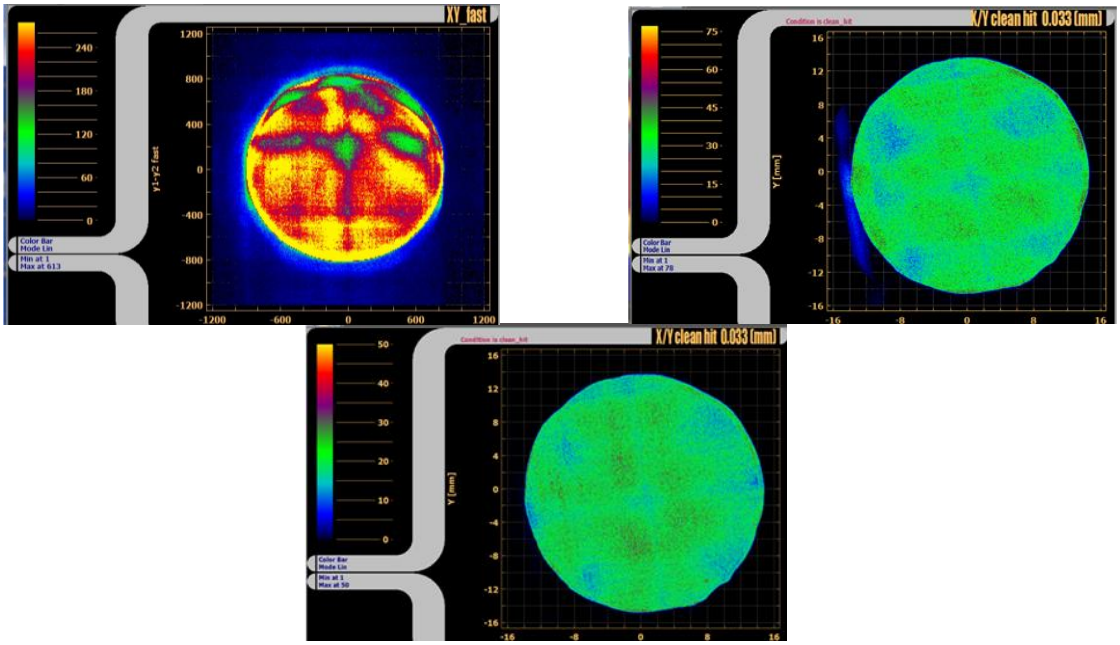

Figure 7: Threshold Adjustment Effects

Once a relatively uniform image of the neutron beam was achieved, an oscilloscope was used to adjust each timing and threshold value to fall just above the level of noise. This allowed for multi-event counting by being able to segregate each pulse into separate events. Pulse pileups are not a concern in this work because the neutron flux and the lower detector efficiency result in count rates lower than the MCP detector system's 1MHz counting rate capability. Any remaining non-uniformity within the image can be easily eliminated in post collection processing.

The anode and MCPs are affected by heat as the vacuum pressure changes as a function of temperature. This caused small deviations within the timing and voltage bias. The pressure began to stabilize after about an hour of use; however, prior to this time, each image required a separate threshold adjustment. Deviations in these radiographs were also able to be corrected by post collection processing by taking an image of the open beam (flatfield) and normalizing radiographs to it. This dynamic system must be either constantly rethresholded to maintain consistency or each individual image must have its own flatfield for normalization. A combination of these two methods has proven to be the most practical way to practically collect large numbers of radiographs in a single time frame.

Some post processing techniques can be used as well in order to aid in the normalization of a series of images. One such technique was done by utilizing the following equation:

$$I(x,y) = \frac{F(x,y) - F(x,y)minimum}{F(x,y)maximum} * k$$

Where I(x,y) is the new intensity of a pixel value, F(x,y) is the original pixel value, and minimum and maximum are the smallest and largest value pixels in the radiograph. K is used as a scaling constant to widen the resulting histogram. This process is shown in Figure 8.

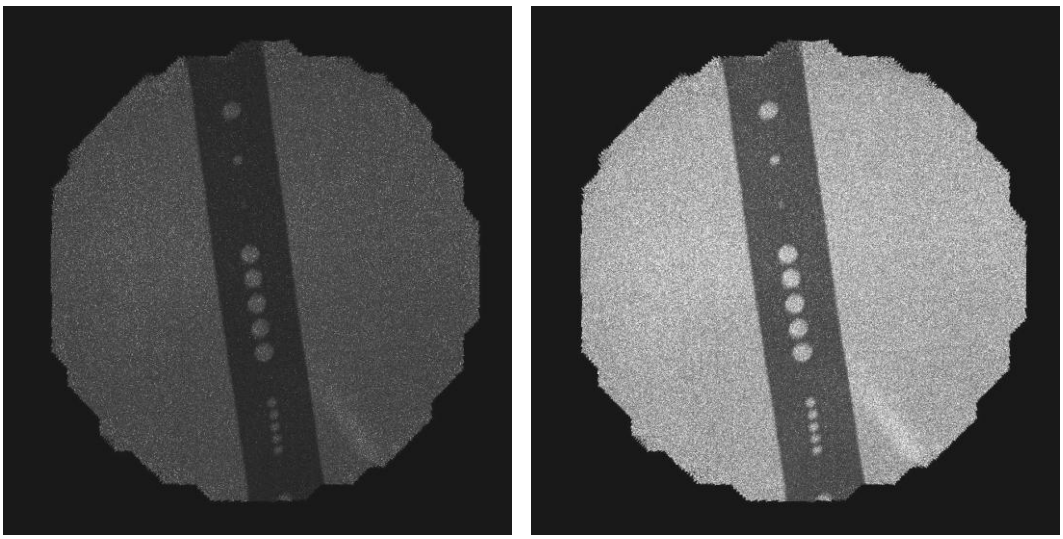

Figure 8: Post acquisition Normalization k=1000(left) k=3000(right)

The benefit of using this method is that it can increase brightness and contrast of the image allowing for small differentiations to stand out. This is the first step in tomography reconstruction because in order to generate a sinogram, discussed further in section 3.6, the different attributes of an object must first be distinguished. Figure 9 illustrates the histograms, or intensity range, of the images shown in Figure 8. It is apparent that with the correct value of K the intensity ratio of a specific radiograph can be spread across the operational range. As this is a sensitive method for correcting a shifting histogram caused by intensity fluctuations, it only works if the entire object is represented within each separate radiograph, which will prove to be important later.

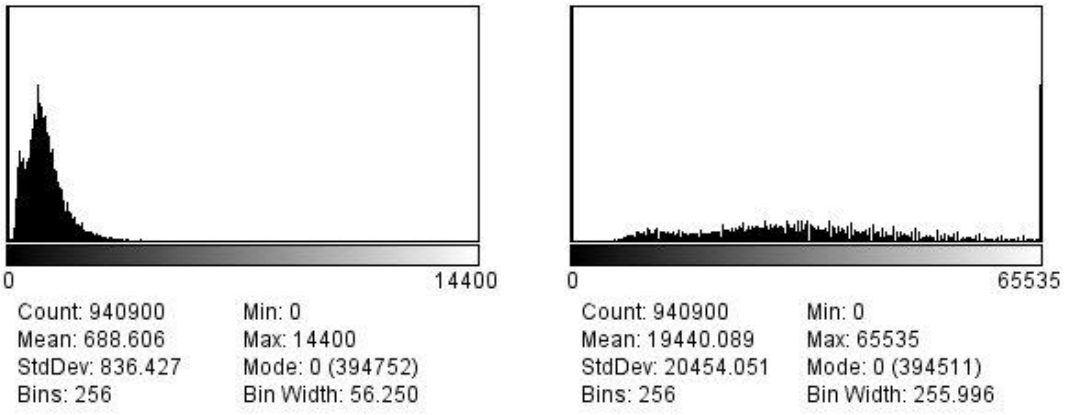

Figure 9: Histograms of Radiographs in Figure 8

3.2 Thermal Neutron Beam

The NRF, where this detector is employed, uses a tangentially orientated beam port, allowing for a predominately thermal neutron beam while minimizing the amount of gamma radiation in the beam. The beam slightly increases in size as it crosses the interior of the NRF. The detector was oriented such that an L/D ratio of 100 was achieved. The beam is an ASTM E545 Category 1 neutron radiography beam with a thermal neutron flux of 4.6E5 ± 5.0E4 n cm^{-2} s^{-1}. Thermal neutrons are most valuable for studying industrial components due to their high penetration through the most widely used industrial materials such as steel, lead, and aluminum along with their high attenuation factors in materials such as ^{10}B.

3.3 Pinhole Masks

The next concern, prior to taking measurements, was to correct for any image distortion. These distortions have a range of causes, ranging from detector geometry to electronic timing. In order to correct for these distortions, a pin hole mask was made with known dimensions. Two such masks were used; the first was an aluminum plate coated with gadolinium

oxide in order to increase neutron absorption for maximum contrast. There were a series of 300 μm in diameter holes drilled throughout the mask spaced 1000 μm apart in grid formation. This mask, shown in Figure 10, proved to have too large of a spacing to adequately correct the image, although temporary corrections were able to be made.

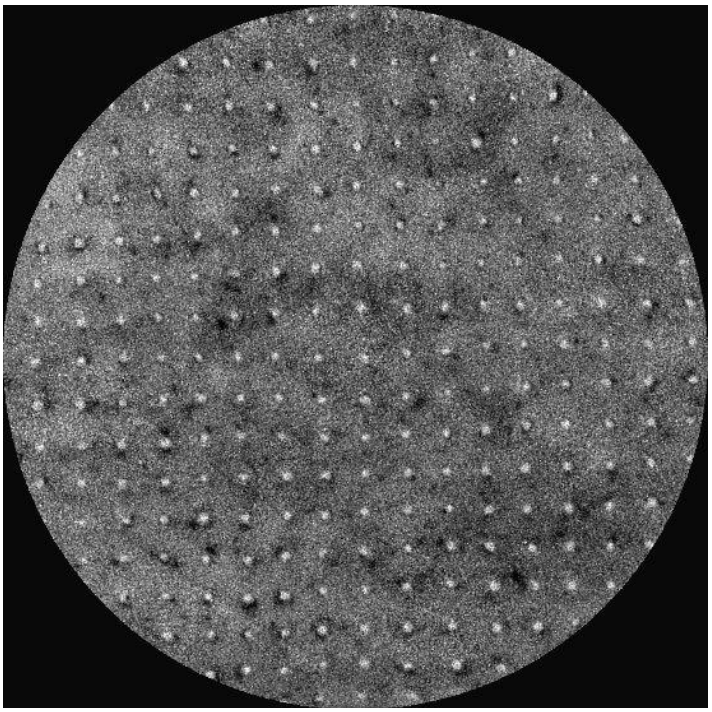

Figure 10: Gd Coated Pinhole Mask With 300 μm Diameter Holes.

Due to the needed correction on the edges of the imaging, where the distortion was most prominent, a second mask with a 20% scale reduction was made. This gadolinium mask with 250 μm diameter holes with a pitch of 1mm was instead used for correction. This mask and its correction are pictured in Figure 11.

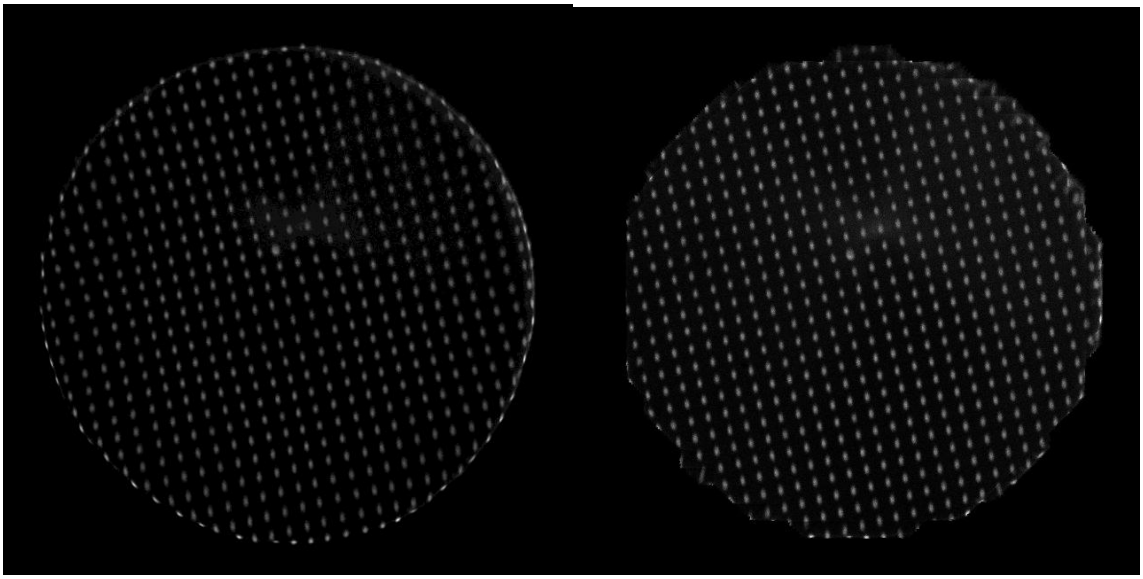

Figure 11: Pinhole Mask Used For Correction, Uncorrected(L) Corrected(R)

This mask was used to create an algorithm to correct future images and allow for accurate measurements to be performed.

3.4 Gamma Sensitivity

A significant factor affecting neutron radiography is the gamma sensitivity of the detector system. Not only is this because many applications of neutron tomography applications are within a gamma field, but also, neutron beams from reactors can never fully filter or collimate out the gammas. Other detectors, such as film and storage phosphors, are easily over exposed in high gamma fields. The MCP detector in use here, is much less sensitive to these low LET ionizing radiations than it is to neutrons.

In order to test this, multiple experiments were done where gamma sources were introduced along with the inherent gamma radiation from the reactor beam. The first test was done using a ^{137}Cs source. The ^{137}Cs source had a strength of 0.02 R hr^{-1} at 1 meter with a gamma energy of 0.667 MeV. Figure 12 shows images taken of a cadmium strip with drilled holes. There was a reference image taken of the strip without the source along with images with the ^{137}Cs source close (~10 cm) to the detector and far (~1 m) from the detector.

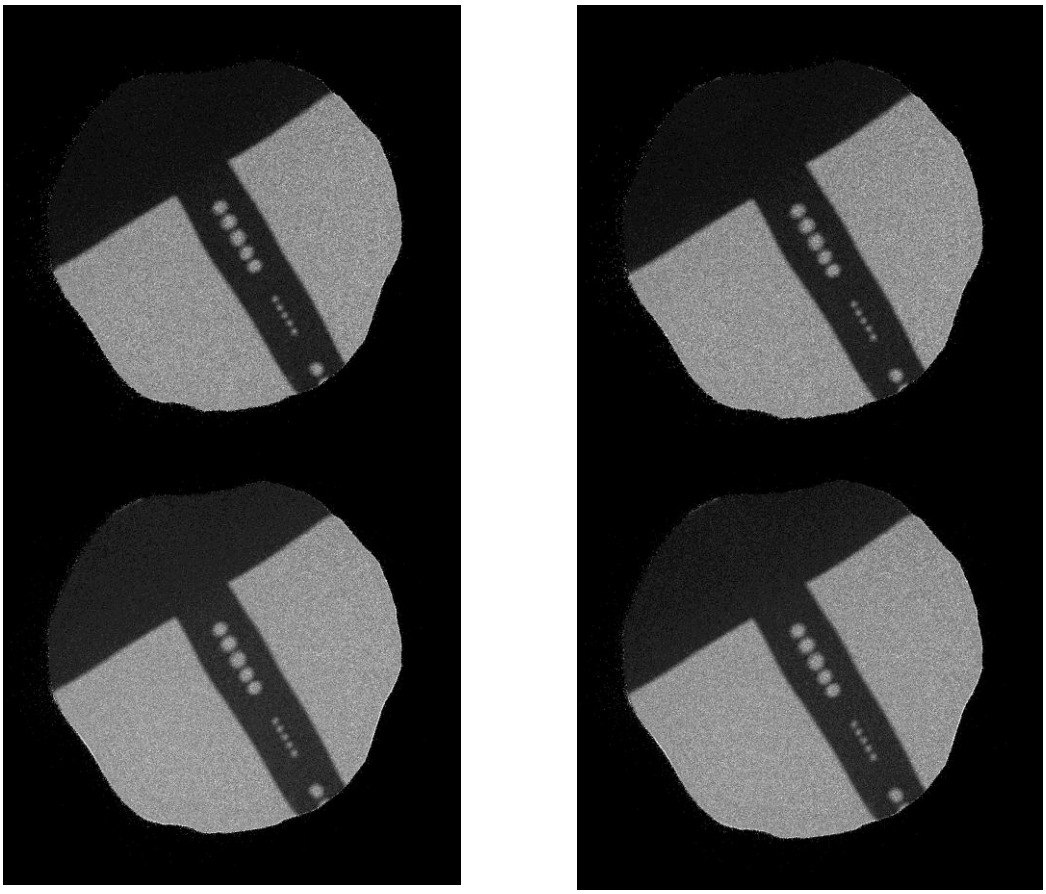

Figure 12: Cs-137 Source At 1 Meter (Upper L) At 0.1 Meter (Bottom L) And Respective Images With Correction (Right)

The next source was antimony, ^{124}Sb, to examine the higher energy gamma. The ^{124}Sb source emits a gamma that is twice the energy of the ^{137}Cs gamma, at 1.3 MeV. The exposure rate was 0.33 R hr^{-1} at 1 meter for this ^{124}Sb source. Figure 13 shows the effect the ^{124}Sb source had on the system at 1 meter from the cadmium strip.

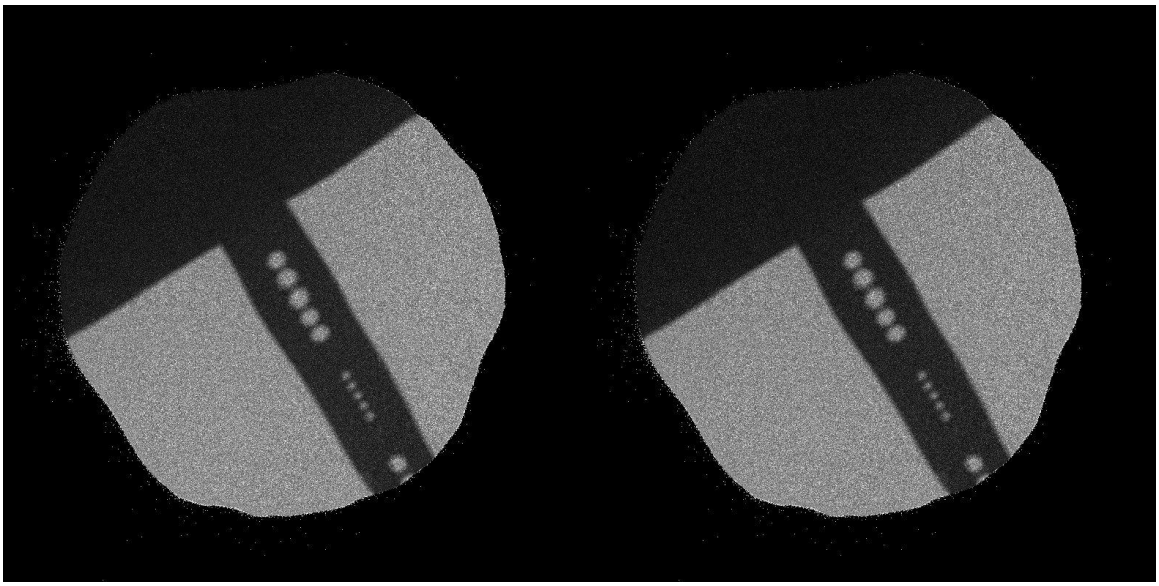

Figure 13: Strip-No Correction(left), With Correction (Right)

Pictured on the left in Figure 13 is the cadmium strip with no correction done for gamma sensitivity, and on the right is the gamma corrected image with the antimony source present. This suggests that the MCP detector system is able to operate in a high gamma environment.

The detector was then sent for maintenance to eliminate the concavity of the images. Upon return, the test was repeated with a new antimony

source. While the same setup was not able to be replicated, the same cadmium strip was imaged with a mixed 357 mCi ^{124}Sb, 4.6 mCi ^{122}Sb source, yielding 0.39 R/hr at 1 meter. This source, placed at a distance of 0.05 meter from the detector, producing the images shown in Figure 14.

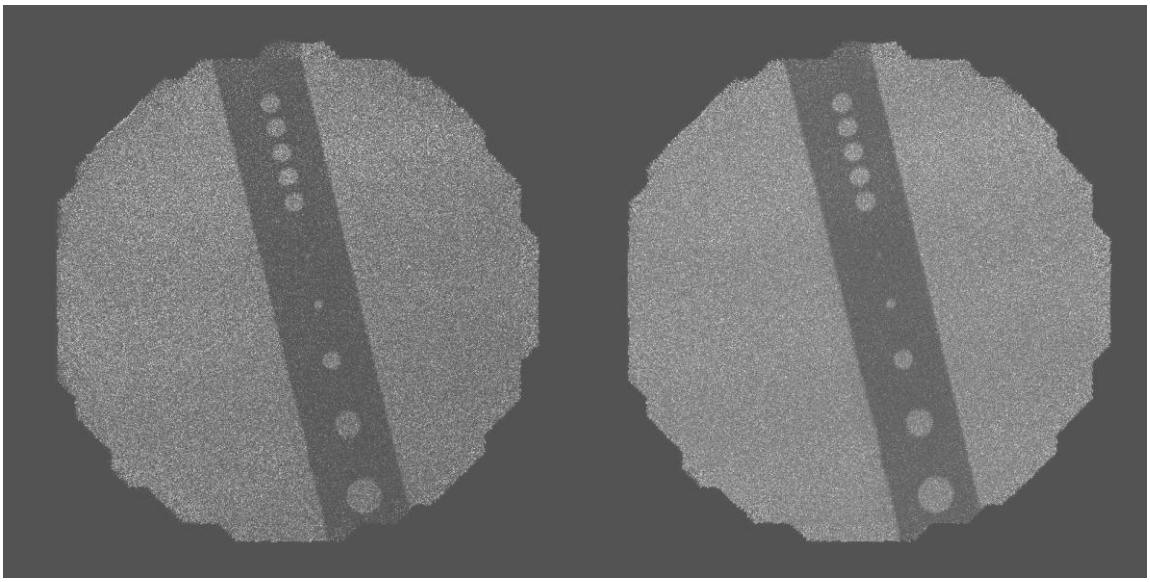

Figure 14: Mixed Antimony Source Result (left) Versus no Source (right)

While there was some gamma sensitivity, Figure 14 suggest that the system can handle high gamma fields. There was an effect. However, it seems to be easily manageable by consistently acquiring flatfield and background images for the correction. If gamma intensity does become a problem, one possibility would be to add a thin sheet of bismuth as a gamma filter in front of the detector due to its high Z and low total absorption and scattering neutron cross section.

3.5 Standards

There are two objects that were used as image quality indicator (IQI) standards as described in the ASTM standard E545. The first was the Beam Purity Indicator (BPI), which was used to determine the relative quality of radiographs obtained by thermal neutron detection. The BPI is a polytetrafluoroethylene block with two boron nitride disks, two lead disks, and two cadmium wires. Its purpose is to allow visual analysis of the radiograph for thermal neutron content of the beam, gamma content, and overall image quality (1). This standard is illustrated below in Figure 15.

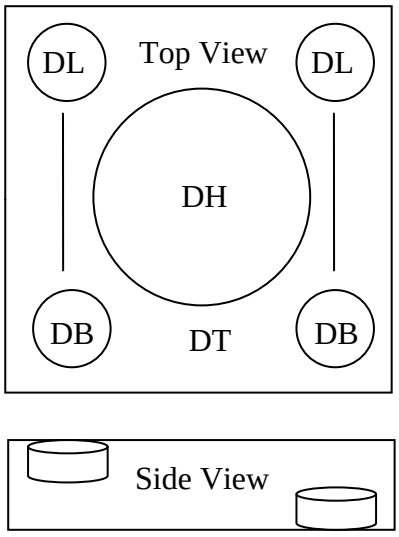

DB: Film densities measured through the images of the boron nitride disks.

DL: Film densities measured through the images of the lead disks.

DH: Film density measured at the center of the hole in the BPI.

DT: Film density measured through the image of the polytetrafluoroethylene.

Δ**DL**: Difference between the DL values.

Δ**DB:** Difference between the two DB values.

Figure 15: BPI Schematic and Quantitative Definitions

The second object in this standard was the Sensitivity Indicator (SI). The purpose of the SI is to pull information from the radiograph regarding overall sensitivity of the detector in both spatial resolution and density discrimination. The SI is a step wedge shaped object containing gaps and holes. This standard is shown in Figure 16.

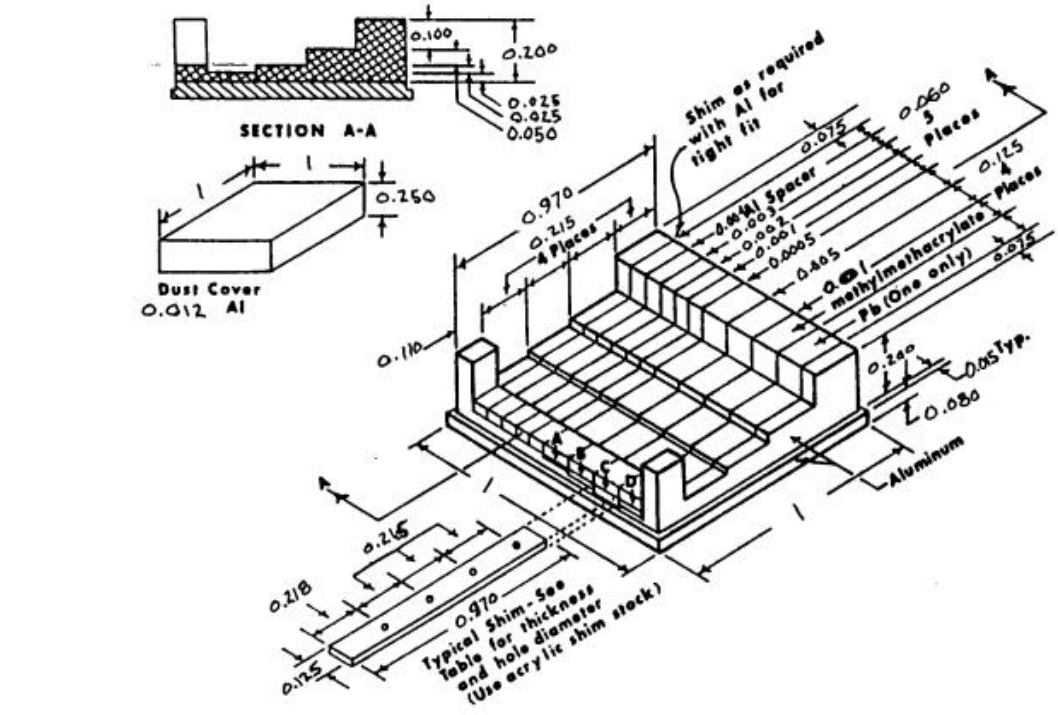

Material — Methylmethacrylate

Shim	Thickness	Hole Diameter
A	0.005	0.005
B	0.010	0.010
C	0.020	0.020
D	0.010	0.010

Figure 16: ASTM Standard S1 Schematic (Units In Inches) (26)

Using the objects imaged for this standard, the Table 1 was used to determine the category of the detector.

Table 1: Neutron Radiography Standards

Category	NC	H	G	S	γ	P
I	65	6	6	5	3	3
II	60	6	6	6	4	4
III	55	5	5	7	5	5
IV	50	4	5	8	6	6
V	45	3	5	9	7	7

This table was tabulated using the following values:

Effective thermal neutron content, NC, where

$$NC = \frac{DB - (highest\ DB + \ \Delta\mathrm{DL})}{DB} * 100$$

Effective scattered content, S, where

$$\mathrm{S} = \Delta\mathrm{DB}/\mathrm{DB} * 100$$

The effective gamma content, γ, where

$$\gamma = (DT - \ lower\ DL/DH) * 100$$

The pair production content, P, where

$$P = (\Delta \mathrm{DL}/DH) * 100$$

The largest visible numbered hole in the SI, H, where

Table 2: ASTM Standard Value "H"

Value of H	1	2	3	4	5	6	7	8	9	10	11	12
Shim	C	C	C	C	B	B	B	B	A	A	A	A

And the smallest gap that is visible at all absorber thicknesses, G, where

Table 3: ASTM Standard Value "G"

Value of G	1	2	3	4	5	6	7
Gap	T	U	V	W	X	Y	Z

In order to collect these radiographs, the BPI and SI should be optimally placed next to one another in the same plane as the detector face in the same image. However, due to size constraints from the detector area and the parallel beam, separate radiographs were taken. The BPI, images shown in Figure 17, were acquired through the recording of a unique flatfield, later divided by the raw image of the BPI, both at one minute exposure times and normalized following the ASTM standard guide.

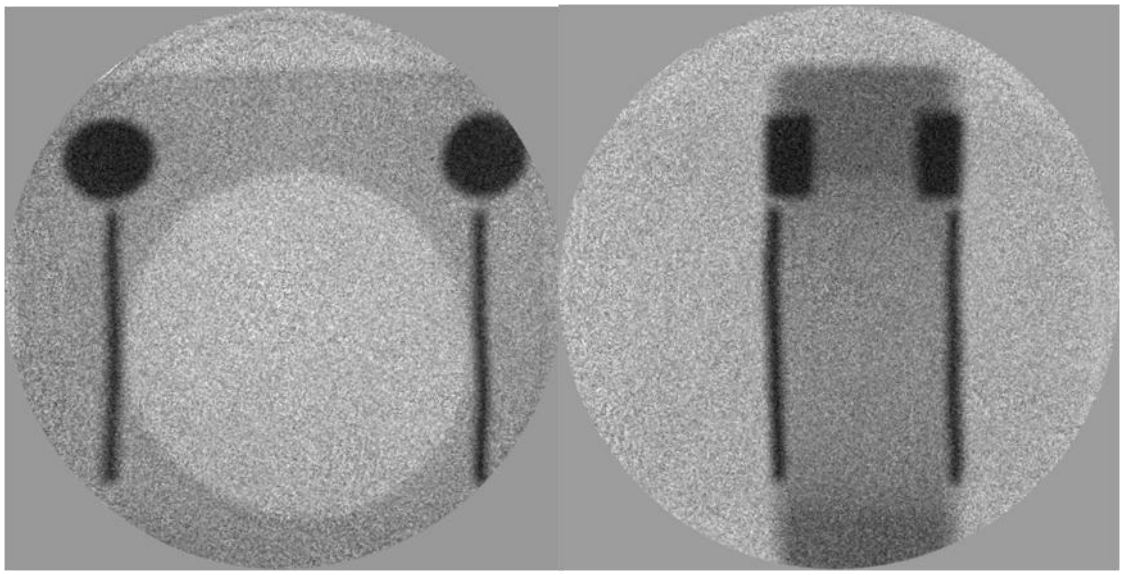

Figure 17: BPI pictured face-on (left) and at 90 degrees (right)

Shown in Figure 18, radiographs of the SI were also taken with their own unique flatfield. However, due to the lower contrast of the material, larger exposure times were required. The raw image was normalized by the flatfield. Once it was normalized, the histogram was equalized to better distinguish characteristics.

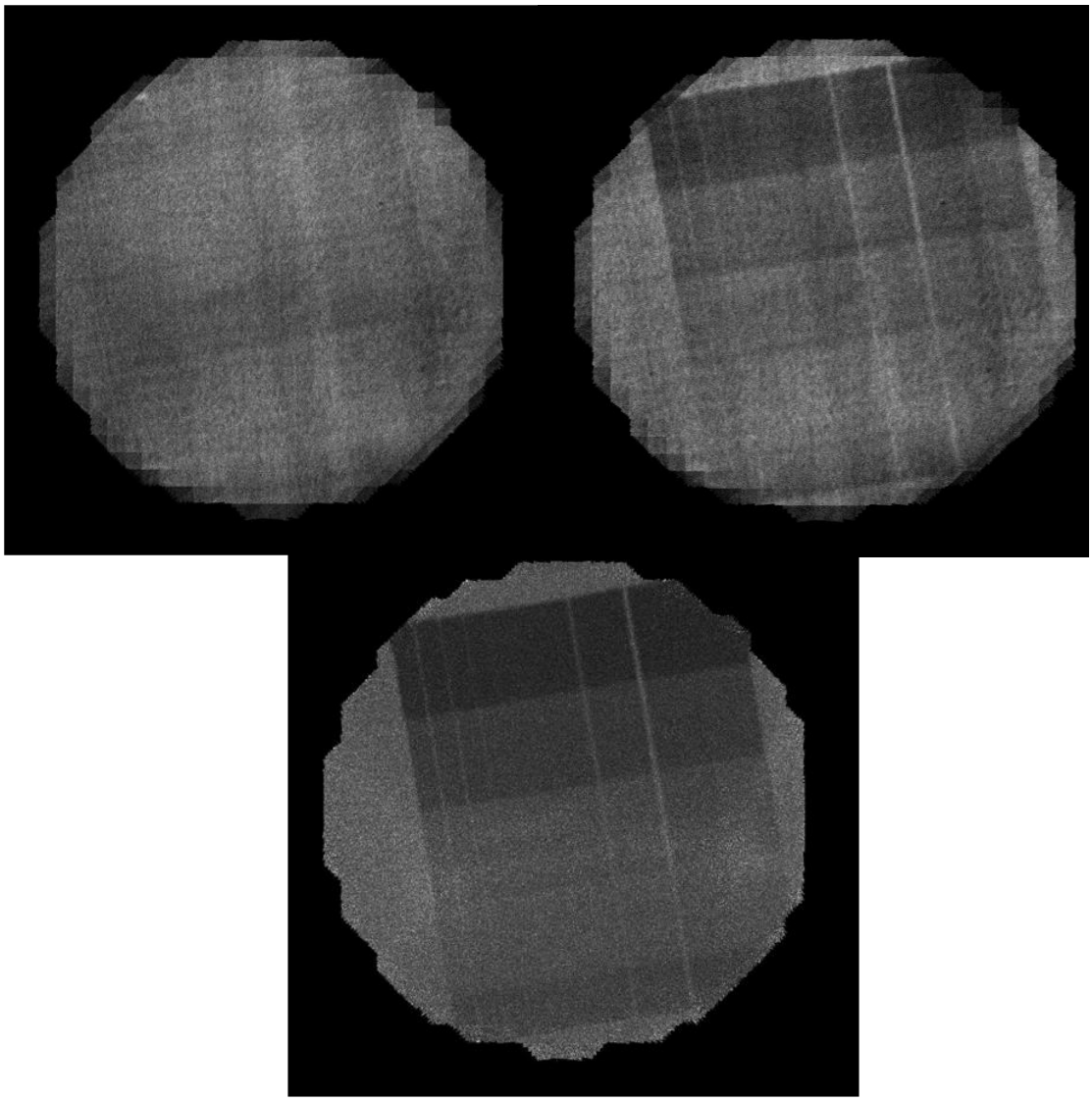

Figure 18: Flatfield (top left) SI (top right), Normalized SI (bottom)

Due to the longer exposure times, the contrast gains were lost because of the dynamic background inherent to the detector system; as the exposure times grow the flatfield is no longer able to properly normalize the image, causing the blur and static in the Figure 18. Through extensive thresholding

of the electronics and varying the voltage bias across the detector, a clearer version was obtained and is shown in Figure 19. On the left is the normalized image, and on the right is a high contrast threshold done post collection in order to sharpen the characteristics of the SI standard.

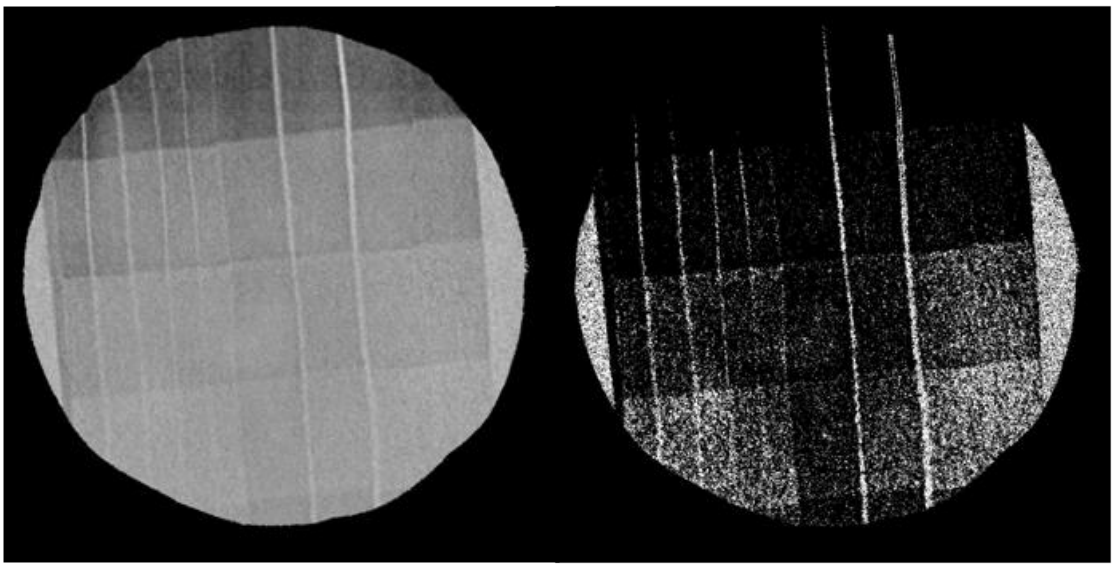

Figure 19: SI Standard (left) Heavily Thresholded (right)

Using these radiographs the standards were analyzed to calculate the data required of Table 1, the results of which can be found in Table 4. The results suggest that the detector falls into a class II radiography system by the ASTM E545 standard.

Table 4: Calculated ASTM Values For MCP Detector

	NC	H	G	S	γ	P
Value	65	6	5	7	4	3
Class	I	II	III	III	II	I

From these standard measurements, primarily the shim thickness visible, the spatial resolution of the detector was estimated to be between 25 and 38 μm depending upon the contrast of object being imaged. This was done by using the SI standard and the information in Figure 16.

3.6 Tomography Reconstruction

When an x-ray passes through a material, it is attenuated. This attenuation is what is used in all x-ray reconstruction. Similarly with neutrons, we look for the loss of neutrons due to absorption and scattering. The concept of reconstruction remains very similar. Both cases result in measuring an intensity drop from the initial beam. Prior to reconstruction it is first required that a large number of projections must be taken over a set of degrees. For a parallel beam, radiographs must be taken over 180 degrees around the object (27).

The next step is to setup the reconstruction process. At every angle, the same pixel will be analyzed. Below, a basic four pixel problem is illustrated.

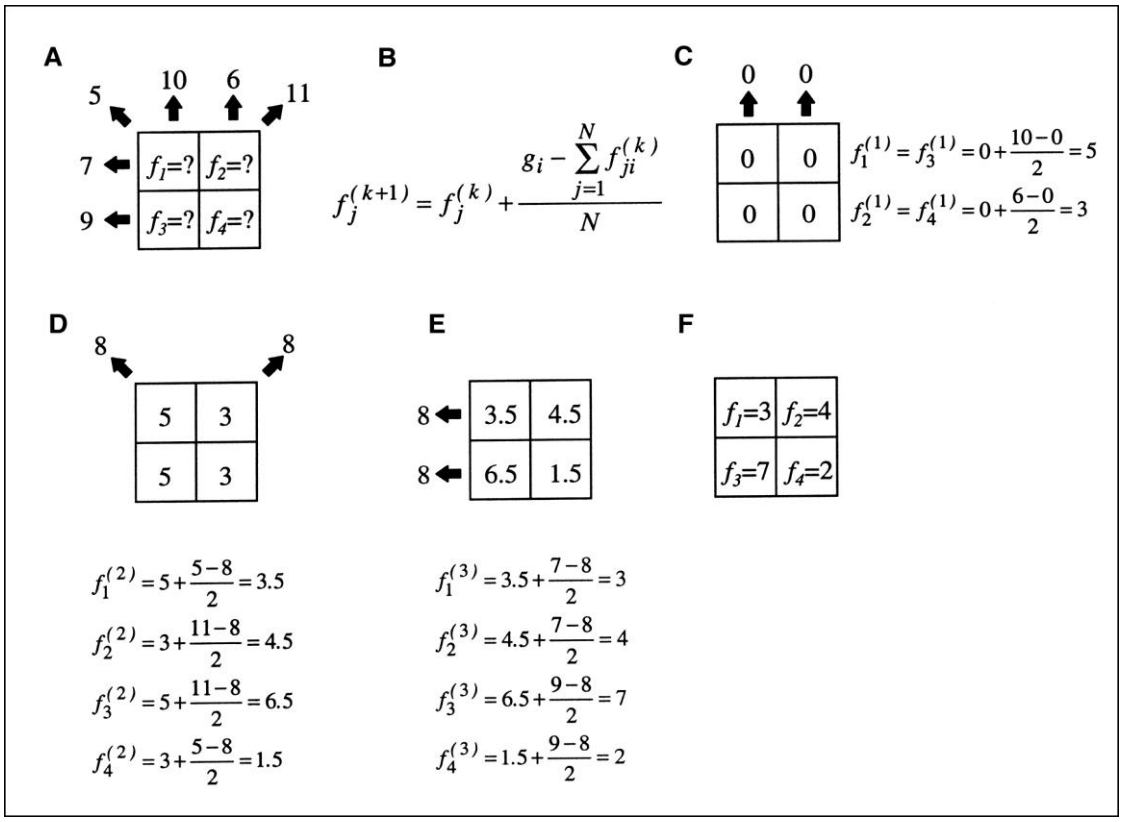

Figure 20: Four Pixel Reconstruction (29)

In this problem, we have a value for every sum from the radiographs, however, the true values, f1-f4, within the object are unknown (A). The first step is assuming a solution exists, typically this value is zero to start (B). By taking the difference between the assumed value and the actual recorded value and averaging them over the row pixels (C), a new value can be assumed (D). From there, this is repeated over every recorded angle to find a solution for every plane of the object. While this is a simplistic view of the

problem it illustrates it well. In practice, when dealing with hundreds of row pixels and projections, this approach is not practical, but the idea remains.

The filtered backprojection algorithm is a way to represent this in a much more encompassing way. Like in the simple problem, it is assumed that each projection represents an independent measurement of the object by using a Dirac Delta function. These independent measurements are placed together to map a single row of pixels into a sinogram. Recall the BPI standard from the previous section. Using the filtered backprojection algorithm, each level can be represented with its own sinogram, illustrated in Figure 21.

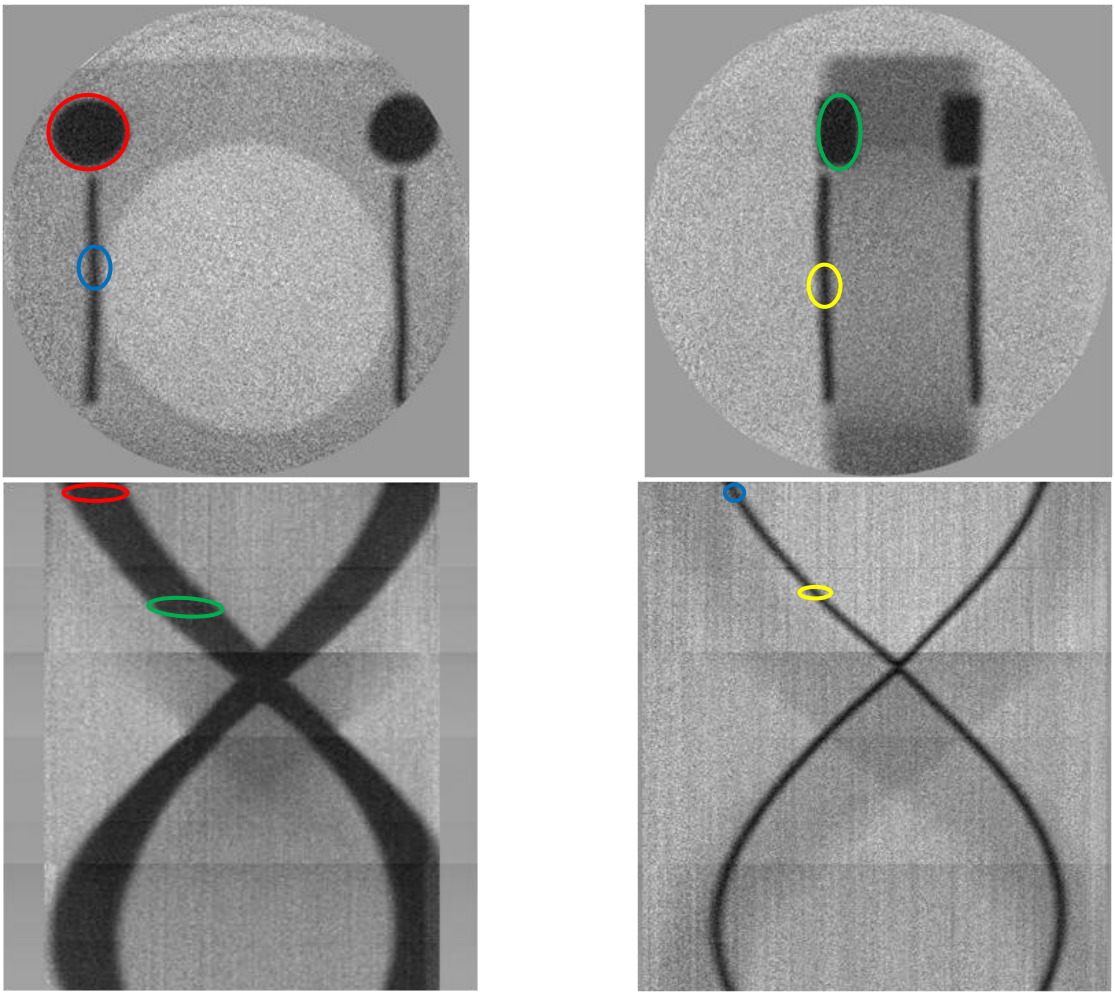

Figure 21: BPI and Respective Sinograms

In Figure 21, it can be seen that as the object rotates, a sinogram can be formed in order to map every level of the object. The disk (marked in red and green) in the BPI, was mapped at every degree of rotation in order to construct its respective sinogram (bottom left). These sinograms represent the solution to the backprojection method. By inputting them into such an algorithm, it

was possible to generate an accurate representation of an object. Figure 22 shows two slices from a computed tomograph of the BPI.

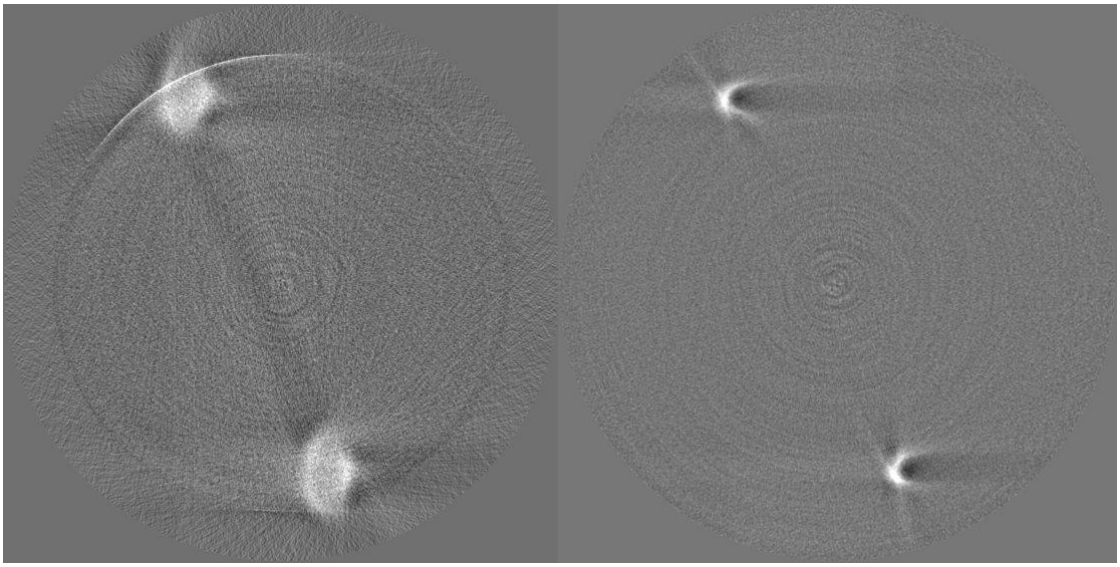

Figure 22: tomograph slices of BPI disk (left) and wire (right)

Because a full tomograph cannot be viewed more than one slice at a time, an isosurface can be rendered by outlining the different features in the tomographic slices. This outlining, or skeleton, of the wire in the BPI is shown in Figure 23.

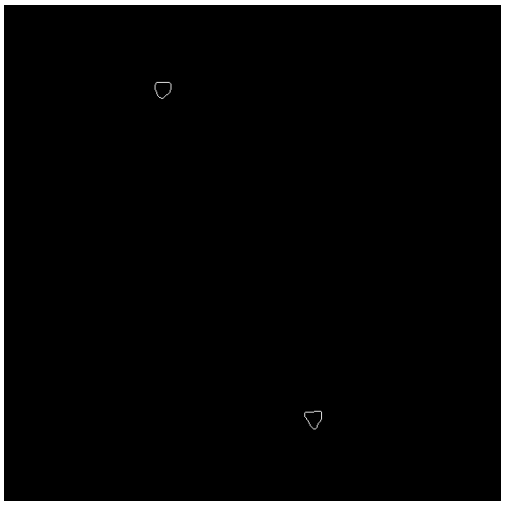

Figure 23: Skeleton of BPI wire

The final step in reconstruction was to combine the skeleton representation from every slice into a full isosurface shown in Figure 24. This results in a 3-dimensional representation of the BPI. From such an image, accurate measurements can be taken on the geometry.

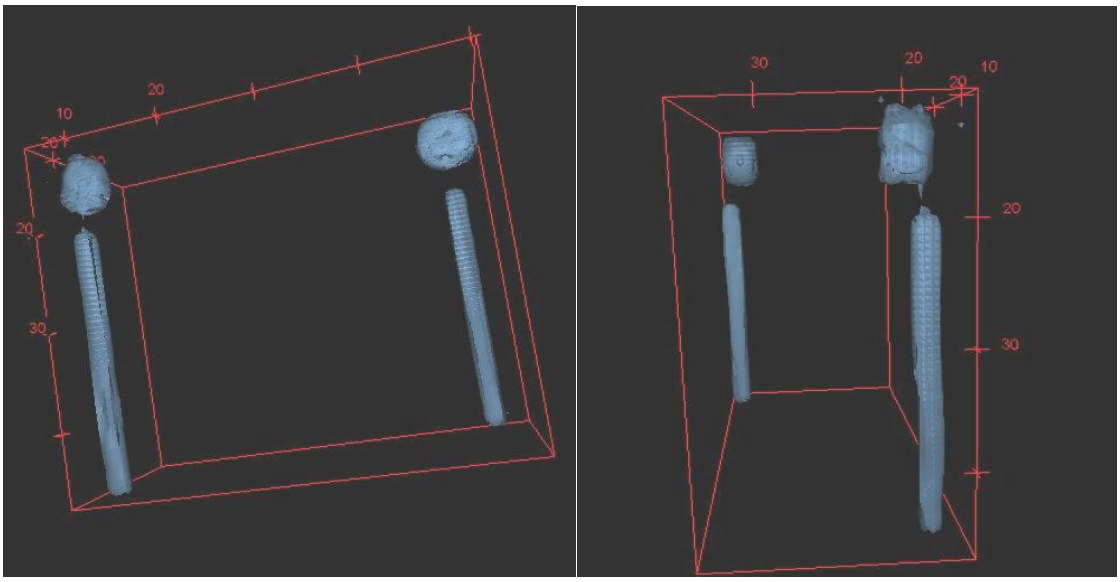

Figure 24: Isosurface of the BPI

3.7 Applications And The AFIP7 Fuel Element

This same tomographic reconstruction technique can be applied to more sophisticated objects. One object of particular interest was the AFIP7 reactor fuel element. This is a long element made up of four seperate fuel plates held together in a bowing congfiguration. This is illustrated in Figure 25 from a front view (top) and a side view (bottom).

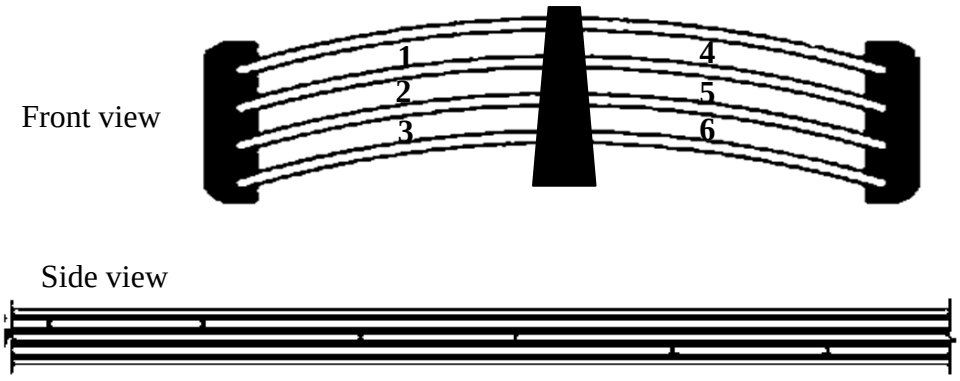

Figure 25: AFIP 7 Mockup

This mockup is made of aluminum. In order to view it using neutron radiography, as aluminum is nearly transparent, a coating of gadolinium oxide was painted along the surface to provide contrast. The images shown in Figure 26 are radiographs taken at 0 an 90 degrees respectively, taken from the side of the element as shown in Figure 25.

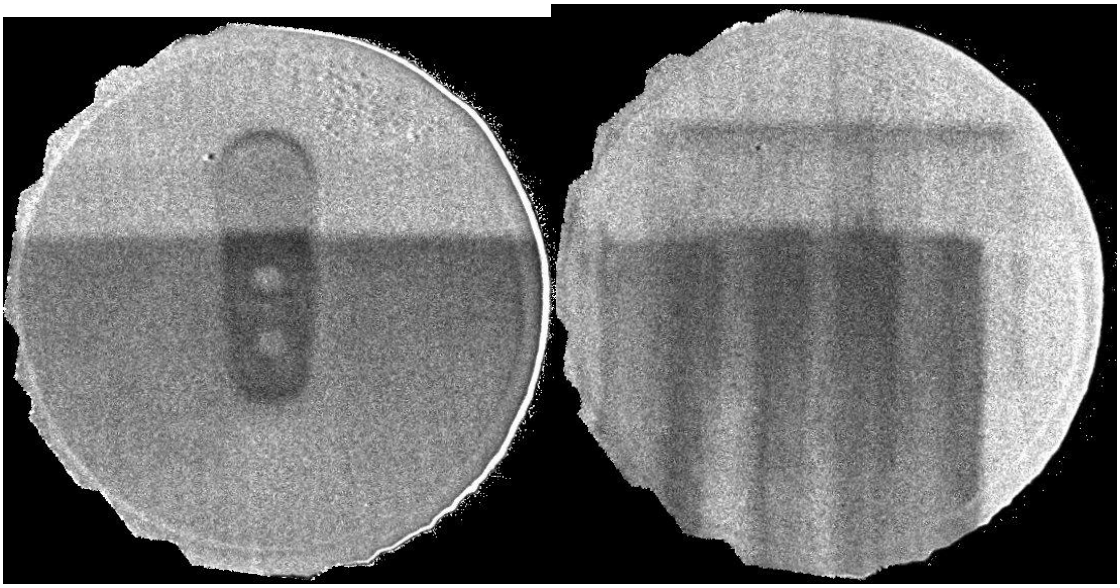

Figure 26: Radiographs of AFIP7 element

From these radiographs, a set of sinograms were able to be created. Two of which are shown in Figure 27. It is important to note how much more complicated the sinograms can get when referencing a complicated geometry instead of a simple object such as the BPI.

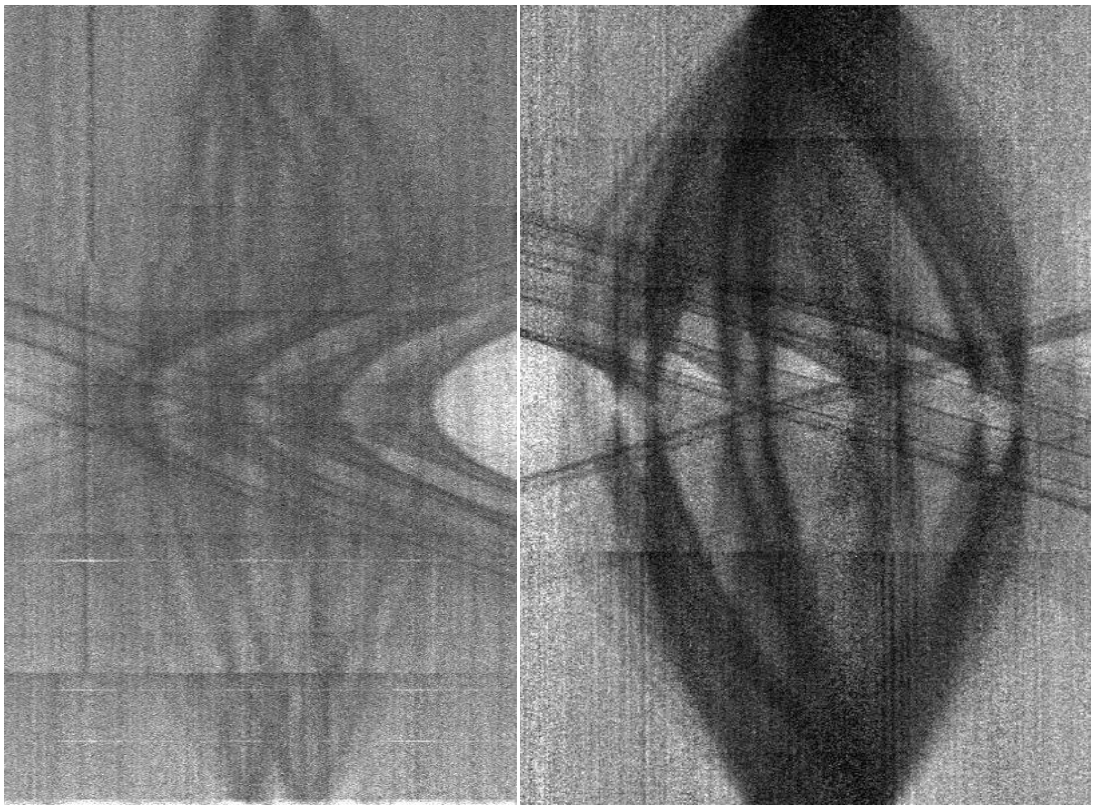

Figure 27: AFIP 7 Sinograms

From this set of sinograms, a tomograph was able to be rendered. However, unlike the previous tomograph, the detail was lacking due to contrast issues. To counter this, the tomographs slices were superimposed onto one another to improve contrast. Figure 28 shows the reconstruction of the element from the front view, and another reconstruction from the side view. Due to this combination of slices, measurements are still able to be taken; however, they will have a larger uncertainty with the seperate locations being condensed into one plane.

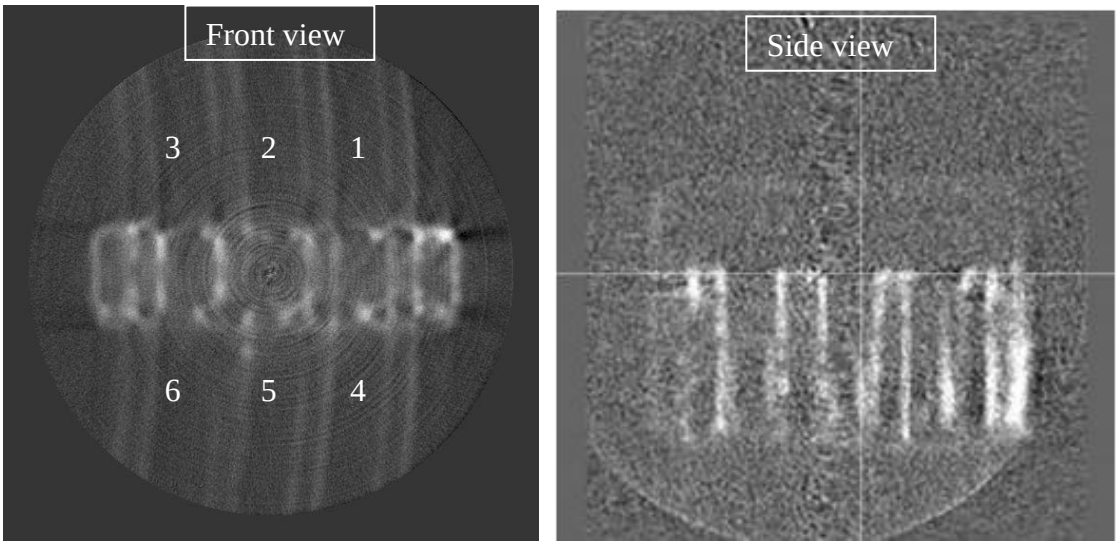

Figure 28: Tomogrpahic Slices of AFIP 7 Euel Element

From these slices, gap width measurements were taken ranging from 0.135 to 0.16 inches depending up upon the location of the measurement. In order to properly test these measurements, a gap width probe was used to check the gap widths in an already proved manner. This probe works as a parallel plate capacitor with the object being measured. By using electrodes placed on the probe and running a constant current through the object, the electrode-object combination record a voltage that is proportional to the gap between the two. These gap measurements yielded the results shown in Figures 29-31.

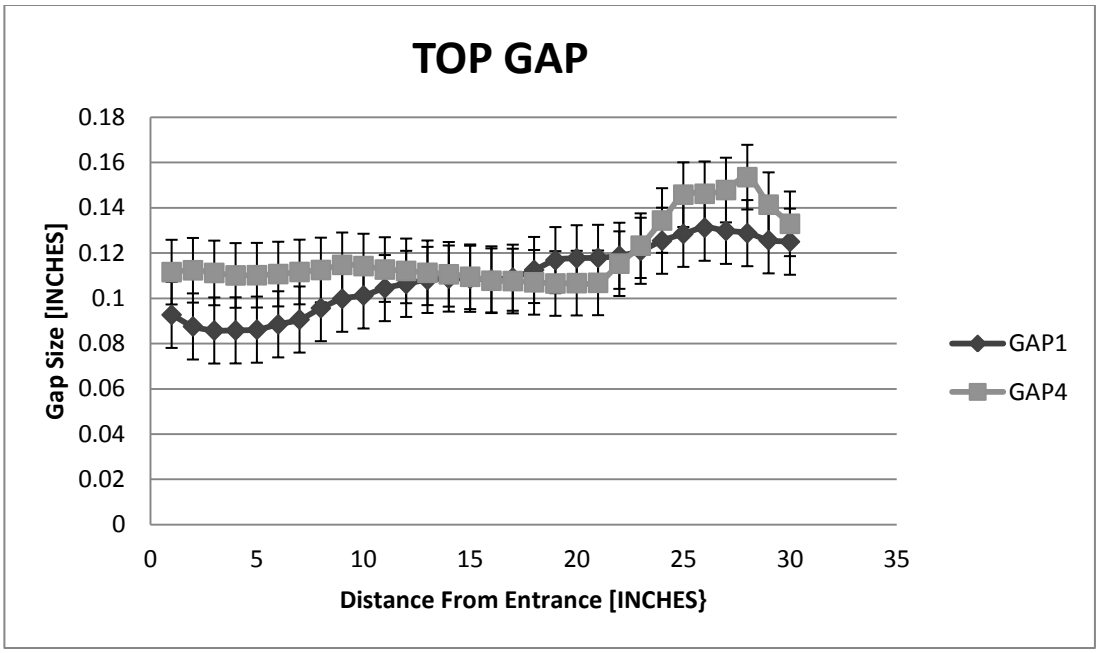

Figure 29:Top AFIP 7 Gap Measurements.

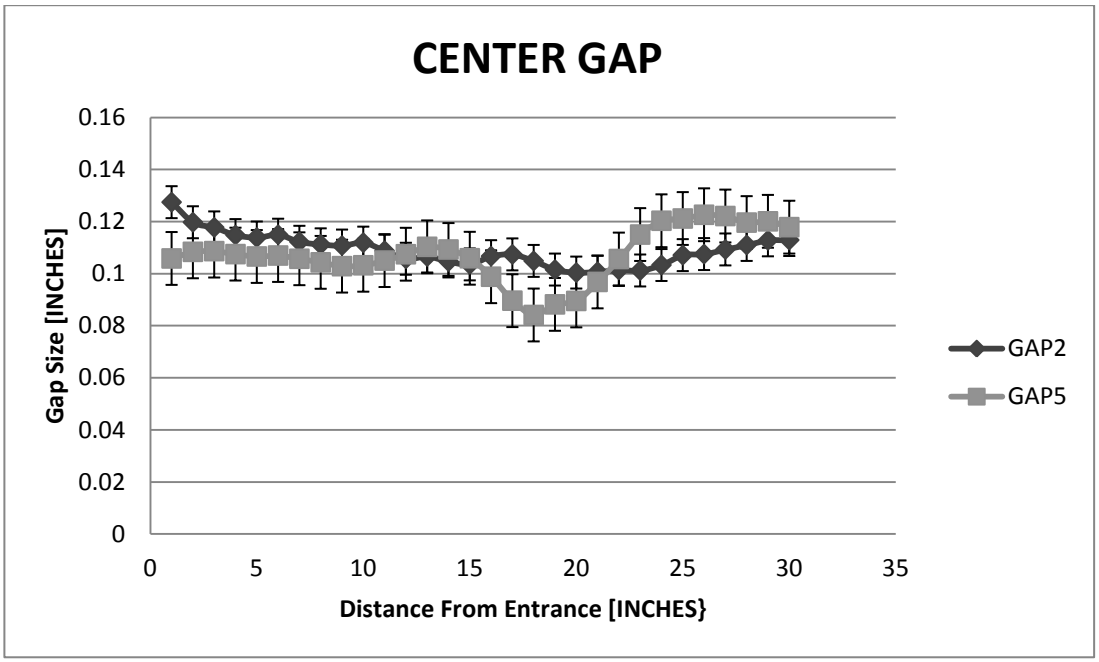

Figure 30: Center AFIP 7 Gap Measurements

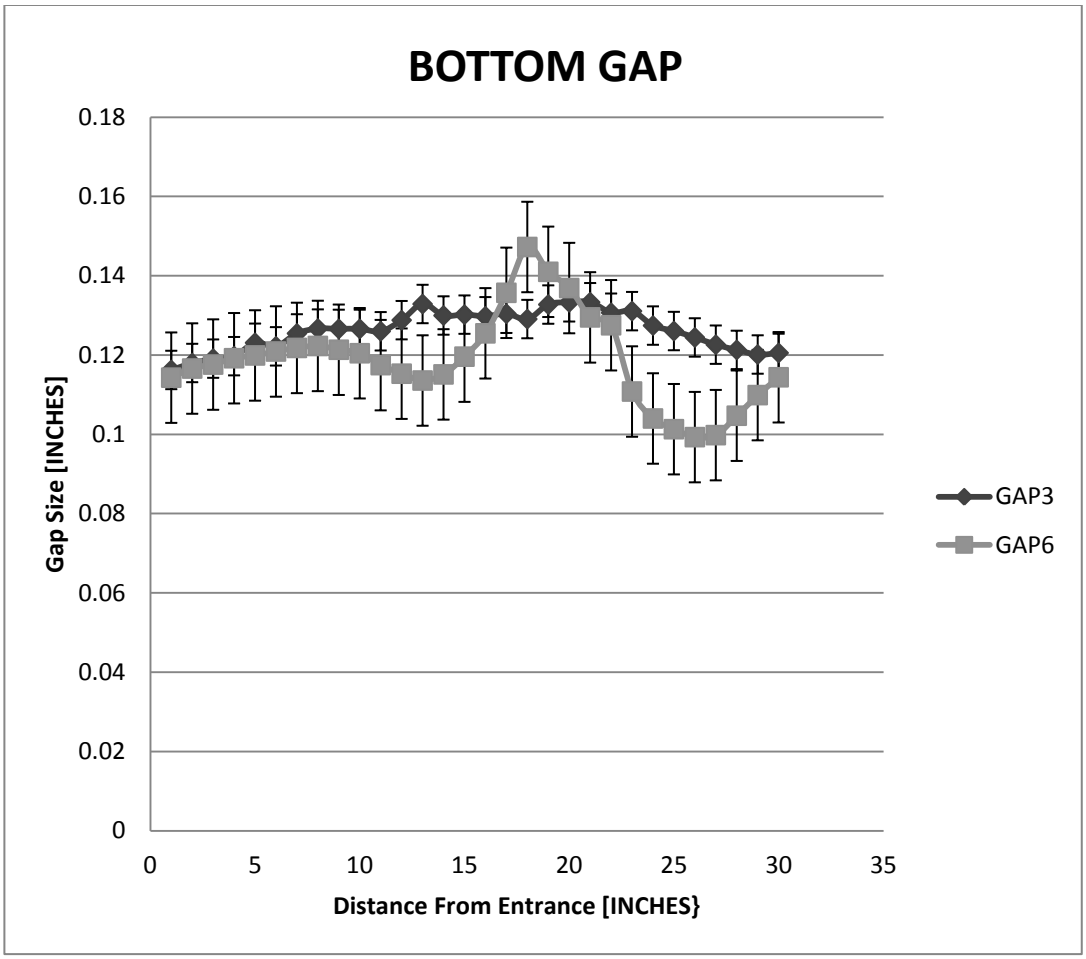

Figure 31: AFIP 7 Bottom Gap Measurements

4 Discussion And Conclusion

The MCP detector developed by NOVA Scientific used for neutron detection uses the reaction $^{10}B(n,\alpha)^{7}Li$ to detect neutrons. This reaction occurs within the few micron thick glass MCP channel walls doped with ^{10}B. The α and ^{7}Li products, moving 180 degrees apart to conserve momentum, pass from the channel wall surfaces into an open MCP channel. These particles, primarily the α, generate a strong electron avalanche and output pulse in the detector. Under the condition that the electronics are properly configured, the probability of initiating an electron avalanche is assumed to be 1. By using a stack of MCPs, the neutron event detection efficiency is near 100%.

By making corrections for distortions, caused by timing issues, using a pinhole masks and imaging objects of known dimensions, it is possible to take accurate measurements of objects being imaged. The spatial resolution has been determined to be maximized at approximately 25 μm. However, the contrast of the material plays a large role in the final resolution and must be taken into account as materials vary. By performing extensive measurements of ASTM standards, it is shown that the detector ranges from category one to a category three neutron sensitive detector.

Because of the extremely high speed, it is possible to perform tomography of specific objects. Due to the small active area of the detector, it is not practical at this time to perform tomography on larger objects. However when viewing objects within the active area, it is not only possible, but much faster than previous attempted methods. While typical tomography procedures require that the images are collected simultaneously and normalized with the same set of background images, this is not feasible with this system. The reasoning for this is the dynamic background intrinsic to the detector. This is countered by segmenting the image collection as much as possible and providing a unique flatfield, or background image, for as many radiographs as can be achieved. Previous methods for normalization work well on objects of smaller sizes. However, when an object is larger than the active area of the detector the dynamic background cannot be corrected post processing due to the subsequent loss of vital information which causes the misrepresentation of geometry.

After comparing the results of the tomography measurements to those of the gap probe measurements, the tomographic measurements resulted in slightly higher values of an overall average of 0.145 Inches versus the gap probe measurements averaging 0.115±0.005 Inches. While this is a 26%

increase, the uncertainty in the tomography measurements can be reduced to obtain better accuracy with his method. One of the main reconstruction issues here is the incorrect normalization of the radiographs prior to the building of the sinograms. This goes back to the dynamic background of the system. Because we are imaging an object with larger area than the active detector area, the normalizing that has worked in previous reconstruction no longer can work here. This is because the normalization assumes that the rescaling is equally represented throughout every image. Where in fact, as the object is viewed at different angles, more of the object is within the active detector area. This causes an intensity shift based upon a different neutron absorption rate along with a shift due to the fluctuation of the detectors background. Because the normalization is being done to counter the latter of the two changes, the first change is lost and indistinguishable after the fact. Thus, once a sinogram is created for reconstruction, the true intensity is lost for some areas and misrepresented in the later steps. This seemingly small change in the view on intensity can largely affect the reconstruction of an object that is thicker or thinner than the actual object being imaged.

In conclusion, the MCP detector used in this study has the resolution and speed required to capably produce both radiographs and tomographs of

useful and competitive quality. The inconsistency of the radiographs caused by the dynamic background forces twice the amount of images to be collected to perform tomography of objects fully viewable in the radiographs. This MCP based detector has a lower efficiency than other systems, approximately 20%, but has already been improved by adding more MCPs.

Future work with this detector is to be done at Idaho National Laboratory. This work will consist of imaging spent nuclear fuel to better test the gamma resistivity and tomography capabilities while viewing materials with high cross sections for neutron interaction. These high cross sections will allow for better contrast. With higher contrast, it may be possible to cut down the number of radiographs required to produce a useful tomograph from hundreds to approximately thirty. Subsequently, this would allow for much faster acquisition times. The dynamic nature of the detector may be drastically improved, or minimized, by pulling a lower vacuum allowing for off gassing within the MCP to be lowered.

5 Appendix A: Thermal Neutron Linear Attenuation Coefficients Using Average Scattering And Thermal Absorption Cross Sections For Naturally Occurring Elements (28)

Element		Cross Section (barns)[a]		Linear Attenuation Coefficient (cm^{-1})[c]
Atomic No.	Symbol	Scattering	Absorption	
1	H	20.49	0.333	gas
2	He	0.76	0.007	gas
3	Li	0.95	70.5	3.31
4	Be	6.15	0.0076	0.76
5	B	4.27	767	101.79
6	C	4.74	0.0035	0.55
7	N	10.03	1.9	gas
8	O	3.761	0.0019	gas
9	F	3.64	0.0096	gas
10	Ne	2.415	0.039	gas
11	Na	3.025	0.53	0.09
12	Mg	3.414	0.063	0.15
13	Al	1.413	0.231	0.10
14	Si	2.0437	0.171	0.11
15	P	3.134	0.172	0.12
16	S	0.9787	0.53	0.06
17	Cl	15.8	33.5	gas
18	Ar	0.647	0.675	gas
19	K	2.04	2.1	0.05
20	Ca	2.93	0.43	0.08
21	Sc	22.4	27.2	1.99
22	Ti	4.09	6.09	0.58
23	V	4.8	5.08	0.71
24	Cr	3.38	3.07	0.54
25	Mn	2.2	13.3	1.24
26	Fe	11.35	2.56	1.18
27	Co	6	37.18	3.93
28	Ni	17.8	4.49	2.04
29	Cu	7.78	3.78	0.98
30	Zn	4.08	1.11	0.34
31	Ga	6.5	2.9	0.48
32	Ge	8.37	2.3	0.47
33	As	5.43	4.5	0.46
34	Se	8.56	11.7	0.74
35	Br	6.1	6.9	0.31
36	Kr	7.5	25	gas
37	Rb	6.4	0.38	0.07
38	Sr	10	1.28	0.20
39	Y	7.67	1.28	0.27
40	Zr	6.4	0.185	0.28
41	Nb	6.37	1.15	0.42
42	Mo	5.59	2.55	0.53
43	Tc	...	20	1.43
44	Ru	6.5	2.56	0.67
45	Rh	5.0	145	10.89
46	Pd	4.2	6.9	0.75
47	Ag	5.08	63.3	4.01
48	Cd	5.6	2520	117.00
49	In	2.45	193.8	7.52
50	Sn	4.909	0.626	0.16

51	Sb	4.2	5.1	0.31
52	Te	3.74	4.7	0.25
53	I	3.54	6.2	0.23
54	Xe	4.3	23.9	gas
55	Cs	20	29.15	0.42
56	Ba	3.42	1.2	0.07
57	La	10.13	8.97	0.51
58	Ce	9	0.63	0.28
59	Pr	2.54	11.5	0.41
60	Nd	16	50.5	1.89
61	Pm	...	8400	251.79
62	Sm	38	5670	171.86
63	Eu	...	4565	94.82
64	Gd	172	48890	1483.88
65	Tb	6.92	23.4	0.95
66	Dy	105.9	940	33.13
67	Ho	8.65	64.7	2.35
68	Er	9	159.2	5.49
69	Tm	6.3	105	3.70
70	Yb	23.4	35.5	1.43
71	Lu	6.8	76.4	2.82
72	Hf	10.3	104.1	5.14
73	Ta	6.12	20.5	1.47
74	W	4.77	18.4	1.46
75	Re	11.3	89.7	6.86
76	Os	15	16	2.21
77	Ir	14.2	425.3	30.86
78	Pt	12.4	10.3	1.50
79	Au	7.84	98.65	6.14
80	Hg	26.5	372.3	16.21
81	Tl	10.01	3.43	0.47
82	Pb	11.26	0.171	0.38
83	Bi	9.3	0.0338	0.26
84	Po	...	...	...
85	At	...	...	...
86	Rn	...	...	gas
87	Fr	...	...	...
88	Ra-226*	...	12.8	0.17
89	Ac-227*	...	890	23.77
90	Th	12.97	7.37	0.62
91	Pa	...	210	8.41
92	U-235	14.3	680.9	33.75
92	U-238	9.38	2.68	0.58
93	Np	...	...	...
94	Pu	...	1756	85.96

6 **Appendix B**: Gap Measurements Using Gap Probe

LEFT SIDE OF FUEL ELEMENT

INCHES FROM ENTRANCE	Mean of Gap 1 Measurements	Mean of Gap 2 Measurements	Mean of Gap 3 Measurements
1	0.09268	0.12744	0.11624
2	0.08756	0.119725	0.118
3	0.08578	0.11775	0.1191
4	0.0858333	0.1148	0.11972
5	0.08615	0.11388	0.1231
6	0.0885	0.11494	0.1222
7	0.09062	0.11222	0.12546
8	0.09566	0.11124	0.12668
9	0.0998	0.110775	0.1266
10	0.10126	0.1119	0.1266
11	0.1045	0.1088	0.126
12	0.10636	0.1057	0.1288
13	0.10812	0.10656	0.13288
14	0.10872	0.10466	0.12998
15	0.10862	0.10354	0.1302

16	0.10836	0.1067	0.12978
17	0.1091	0.10738	0.13042
18	0.1125	0.104875	0.12908
19	0.11686	0.10155	0.13274
20	0.11768	0.1004	0.1333
21	0.11786	0.1007	0.133325
22	0.118775	0.1014	0.13068
23	0.12098	0.1012	0.13108
24	0.12542	0.1033	0.12744
25	0.12848	0.1071	0.12606
26	0.13118	0.1075	0.12444
27	0.1298	0.10928	0.12262
28	0.12878	0.111	0.1213
29	0.12562	0.11278	0.12014
30	0.125	0.1129	0.12054
STDV	0.014602414	0.006138713	0.004844853

RIGHT SIDE OF FUEL ELEMENT

INCHES FROM ENTRANCE	Mean of Gap 4 Measurements	Mean of Gap 5 Measurements	Mean of Gap 6 Measurements
1	0.11156	0.10582	0.1143
2	0.112375	0.10836	0.1166
3	0.1112	0.10864	0.1176
4	0.1101	0.107483333	0.1192
5	0.1102	0.106575	0.1199
6	0.1107	0.10695	0.1209
7	0.11162	0.1057	0.1218
8	0.1125	0.10432	0.1223
9	0.114775	0.10286	0.12134
10	0.114233333	0.1032	0.12046
11	0.1127	0.105	0.11746
12	0.1121	0.10744	0.1153
13	0.11126	0.11028	0.11358
14	0.1106	0.10926	0.11512
15	0.1095	0.1059	0.1196
16	0.10776	0.0988	0.12548

17	0.10762	0.0896	0.1357
18	0.10706	0.0841	0.14726
19	0.10654	0.08818	0.141
20	0.1067	0.0895	0.1369
21	0.106825	0.0968	0.1295
22	0.1153	0.1056	0.12752
23	0.12324	0.115	0.1108
24	0.13436	0.1203	0.104
25	0.14578	0.12116	0.1013
26	0.14616	0.1226	0.0993
27	0.14782	0.12212	0.0998
28	0.15352	0.1196	0.1047
29	0.14136	0.12008	0.1099
30	0.1329	0.11784	0.1144
STDV	0.014279857	0.01014826	0.011406643

7 **Appendix C**: Standards And Equipment

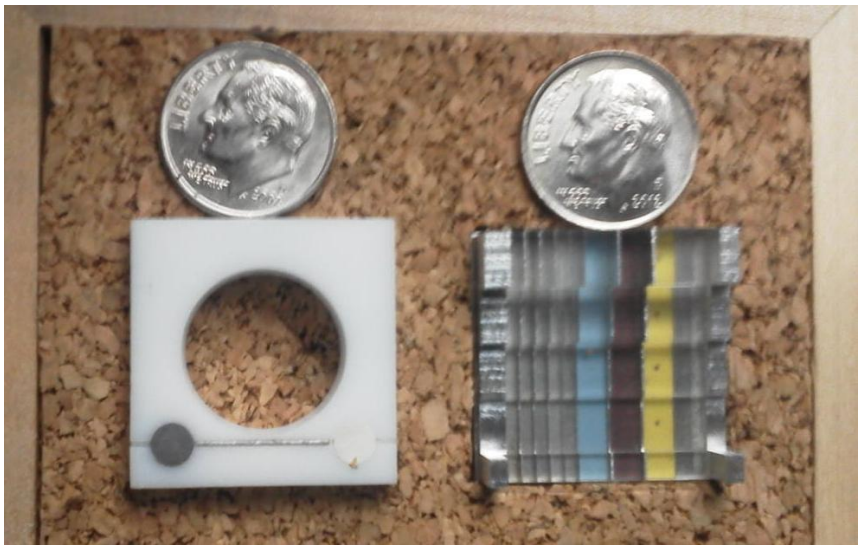

Figure 32: BPI Standard (Left) SI Standard (Right)

Figure 33: Vacuum Pump

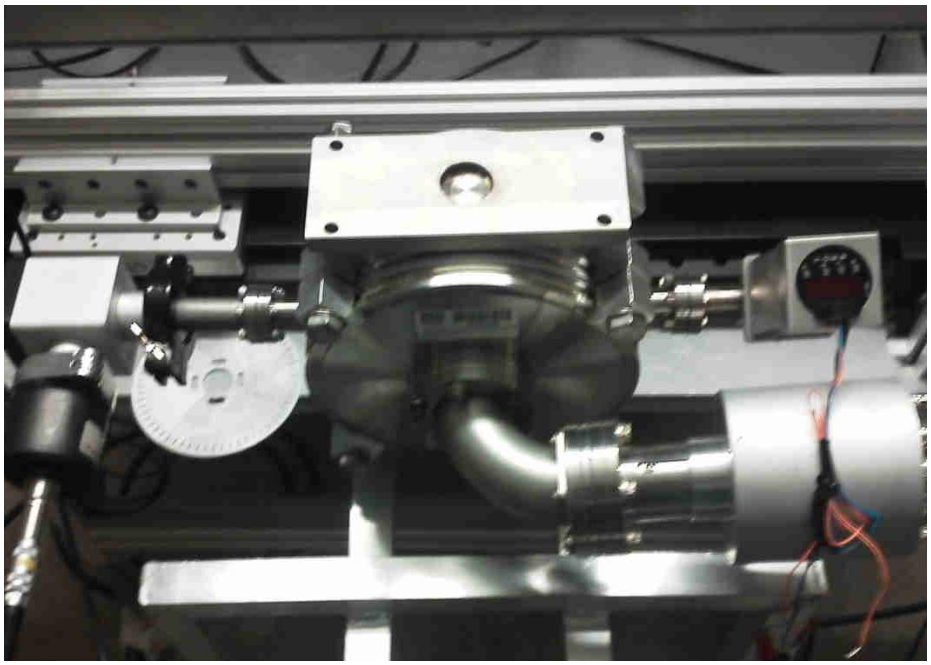

Figure 34: MCP Detector

Figure 35: AFIP 7 Mock Element in Front of MCP Detector

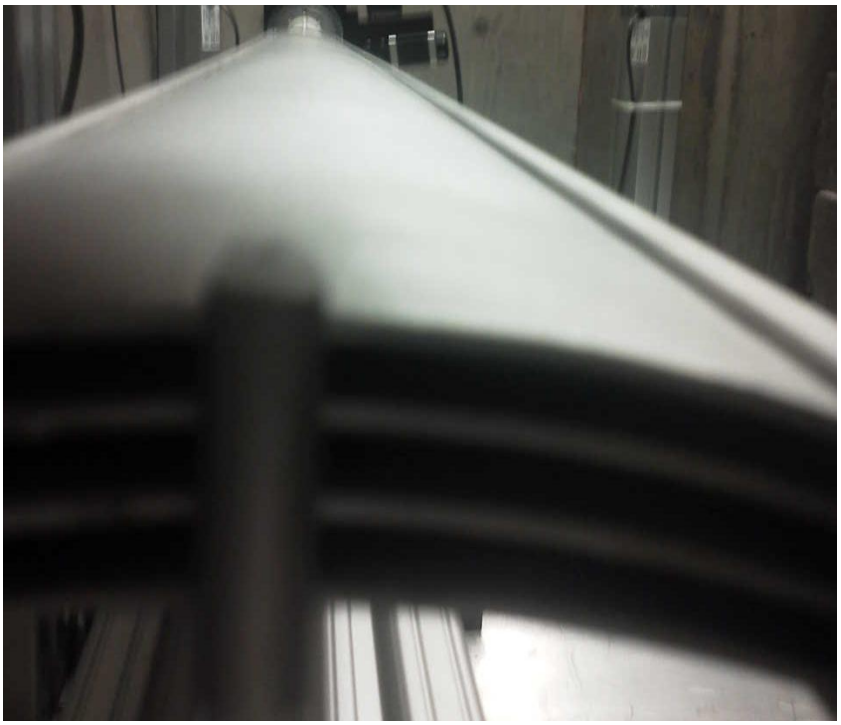

Figure 36: AFIP 7 Element on Rotational Stage

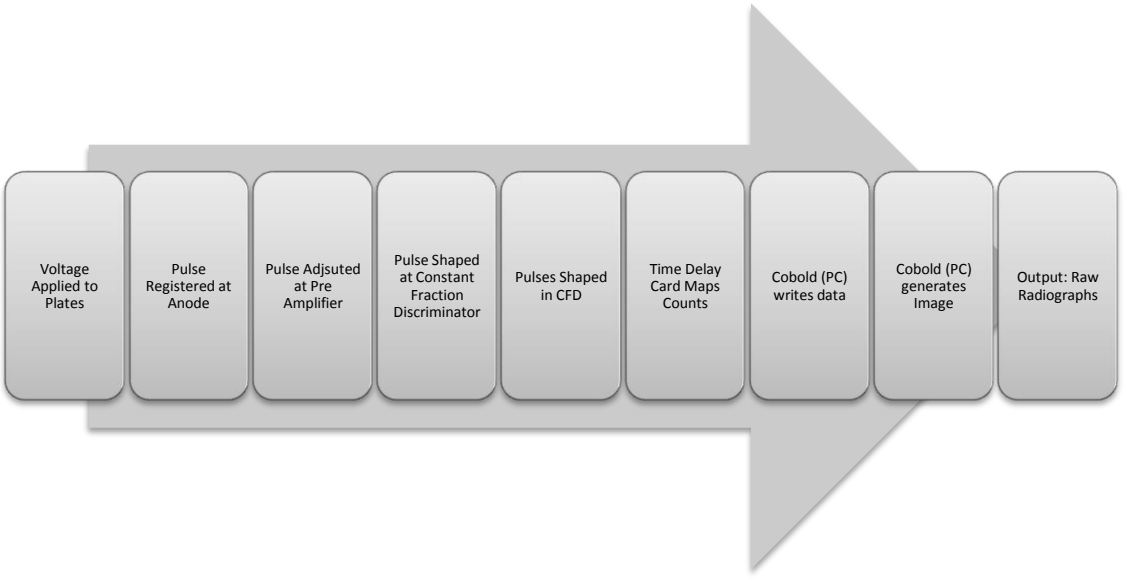

Figure 37: Electronic Process

8 Bibliography

1. INTERNATIONAL, ASTM. Standard Test Method for Determining Image Quality in Direct Thermal Neutron Radiogrpahic Examination. 2010. E5454-05.

2. E Rutherford, proc Roy soc, a 97, 374-400, 1970.

3. W.D. Harkins, Natural systems for the classification of isotopes…,J Am Chem soc, 43, 10038-1060,1921.

4. J C, possible existence of a neutron, nature 129, 312, 1932.

5. JC. The Existence of a Neutron proc roy soc. 1932. 692-708.

6. Kallman, H. Neutron Radiography Research 1. 1948. 254.

7. Klann, Raymond T. A System for Fast Neutron Radiogrpahy. Crete, Greece : Fifth International Conference on Applications of Nuclear Techniques , June 1996 .

8. Barton, JP. Proceedings of the 'World Conferences on Neutron radiography'. Paris, France : s.n., 1986.

9. Peter, Oz. Neutronen-Durchleuchtung, Naturforsch. 1946. Vol. 1. 557.

10. Thewlis, J. Neutron Radiography. *British Journal of Applied Physics.* Harwell England : s.n., 1956. Vol. 7.

11. Berger, H. Proceedings Symposium on Physics and Non-Destructive Testing. Argonne Illinois : Argonne National Laboratory, 1960. Vols. Anl-6346.

12. Neutron Radiography: Methods, Capabilities, and Applications. new York : Elsevier publishing company, 1965.

13. Hawkesworth, M.R. Radiography With Neutrons Conference September, 1973. s.l. : British Nuclear Energy Society, 1975.

14. Berger, H. Practical Applications Of Neutron Radiography And Gauging. 1976. ASTM STP 586.

15. JP Barton, J Farny, J Person, H Rottger. Introductory Remarks Neutron Radiography: Proceedings At The Second World Conference On Neutron Radiography, Paris, France. Dordrecht, Holland : s.n., 1987.

16. Sulcoski, Js Brenizer and MF. Real Time Neutron Radiography at the University of Virginia in use and Development of Low and Medium Flux Reactors. Harling, OK : s.n., 1984.

17. Domanus, J.C. Neutron Radiography, Techniques and Applications . Roskilde, Denmark : Risø National Laboratory, October 1987 .

18. Mesot, J. Neutron News. New York : Taylor & Francis, 1992. Vol. Vol. 3 No. 3.

19. Anderson, Ian. Neutron Imaging and Applications. New York, NY: Springer Science, 2009. p50. Print.

20. Leeman, E.H. Nuclear Instrumentation Methods. 2007.

21. D.S Husey, D.L Jackson, et al. New neutron imaging facility at the NIST. Gaithersburg, MD : National Institute of Standards and Technology, 2008. Vol. 542, 1-3.

22. S. Sutiarso, B. Bharoto, and A. Fahrurrozi. Development of Three Dimensional Neutron Tomography at BATAN's RSG-GAS Reactor. s.l. : National Nuclear Energy Agency of Indonesia (BATAN) , 2012.

23. Oswald H. Siegmund, John V. Vallerga, Anton S. Tremsin, Jason Mcphate, Bruce Feller. High spatial resolution neutron sensing microchannel plate detectors. *Nuclear Instruments and Methods in Physics Research Section A: Accelerators, Spectrometers, Detectors and Associated Equipment.* 2007. Vol. 576, 1.

24. Anton S. Tremsin, W. Bruce Feller, R. Gregory Downing. Efficiency optimization of microchannel plate (MCP) neutron imaging detectors. *Nuclear Instruments and Methods in Physics Research Section A: Accelerators, Spectrometers, Detectors and Associated Equipment.* 2005. Vol. 539, 1-2.

25. The IAEA Technical Meeting on Regional Research Reactor Users' Networks (RRUNs): Advances in Neutron Imaging. Serpong, Jakarta, Indonesia : IAEA, 2013.

26. INTERNATIONAL, ASTM. Standard Practice for Fabrication of Neutron Radiographic Sensitivity Indicators. 2013. Vol. 3.03. E2023-99.

27. inCT. Octopus Manual. Ghent, Belgium : s.n., 2008. Vol. 8.5.

28. International, ASTM. Standard Practices for Thermal Neutron Radiography of Materials. 2008. E748 – 02.

29. Bruyant, Philippe P. Analytic and Iterative Reconstruction Algorithms. *Nuclear Methods.* Lyon, France : Nuclear Spectroscopy and Image Processing Research Group, 2002.